

Power Battery Detection

Xiaoqi Zhao¹ · Peiqian Cao² · Chenyang Yu² · Zonglei Feng³ ·
Lihe Zhang² · Hanqi Liu⁴ · Jiaming Zuo⁴ · Youwei Pang⁵ ·
Jinsong Ouyang¹ · Weisi Lin⁵ · Georges El Fakhri¹ ·
Huchuan Lu² · Xiaofeng Liu¹

<https://github.com/Xiaoqi-Zhao-DLUT/X-ray-PBD>

Received: date / Accepted: date

Abstract Power batteries are essential components in electric vehicles, where internal structural defects can pose serious safety risks. We conduct a comprehensive study on a new task, power battery detection (PBD), which aims to localize the dense endpoints of cathode and anode plates from industrial X-ray images for quality inspection. Manual inspection is inefficient and error-prone, while traditional vision algorithms struggle with densely packed plates, low contrast, scale variation, and imaging artifacts. To address this issue and drive more attention into this meaningful task, we present PBD5K, the first large-scale benchmark for this task, consisting of 5,000 X-ray images from nine battery types with fine-grained annotations and eight types of real-world visual interference. To support scalable and consistent labeling, we develop an intelligent annotation pipeline that combines image filtering, model-assisted pre-labeling, cross-verification, and layered quality evaluation. We formulate PBD as a point-level segmen-

tation problem and propose MDCNeXt, a model designed to extract and integrate multi-dimensional structure clues including point, line, and count information from the plate itself. To improve discrimination between plates and suppress visual interference, MDCNeXt incorporates two state space modules. The first is a prompt-filtered module that learns contrastive relationships guided by task-specific prompts. The second is a density-aware reordering module that refines segmentation in regions with high plate density. In addition, we propose a distance-adaptive mask generation strategy to provide robust supervision under varying spatial distributions of anode and cathode positions. Without any bells and whistles, our segmentation-based MDCNeXt consistently outperforms various other corner detection, crowd counting and general/tiny object detection-based solutions, making it a strong baseline that can help facilitate future research in PBD. Finally, we provide a detailed discussion of future directions and challenges for research in power battery detection.

Keywords Power Battery Detection · Benchmark · Point-level Segmentation · Multi-dimensional Clues · State Space Modeling

¹ Yale University, USA

² Dalian University of Technology, China

³ Volkswagen Automotive Co., Ltd

⁴ X3000 Inspection Co., Ltd

⁵ Nanyang Technological University, Singapore

Lihe Zhang and Youwei Pang are the corresponding authors.

E-mail:

xiaoqi.zhao@yale.edu

zhaoxq.cv@gmail.com

zhanglihe@dlut.edu.cn

lartpang@gmail.com

xiaofeng.liu@yale.edu

This work was supported by the National Natural Science Foundation of China under Grant 62431004 and 62276046.

1 Introduction

With the rapid adoption of electric vehicles (EVs), Fig. 1(a) shows that EV market share has grown from around 1% to over 20% in the past five years, with 17.1 million units sold globally in 2024 [26, 48]. The power battery serves as the sole energy source for EVs, directly influencing their performance, range, and safety [85]. As shown in Fig. 1(b), the battery pack contributes nearly 35% of total manufacturing cost, underscoring its crit-

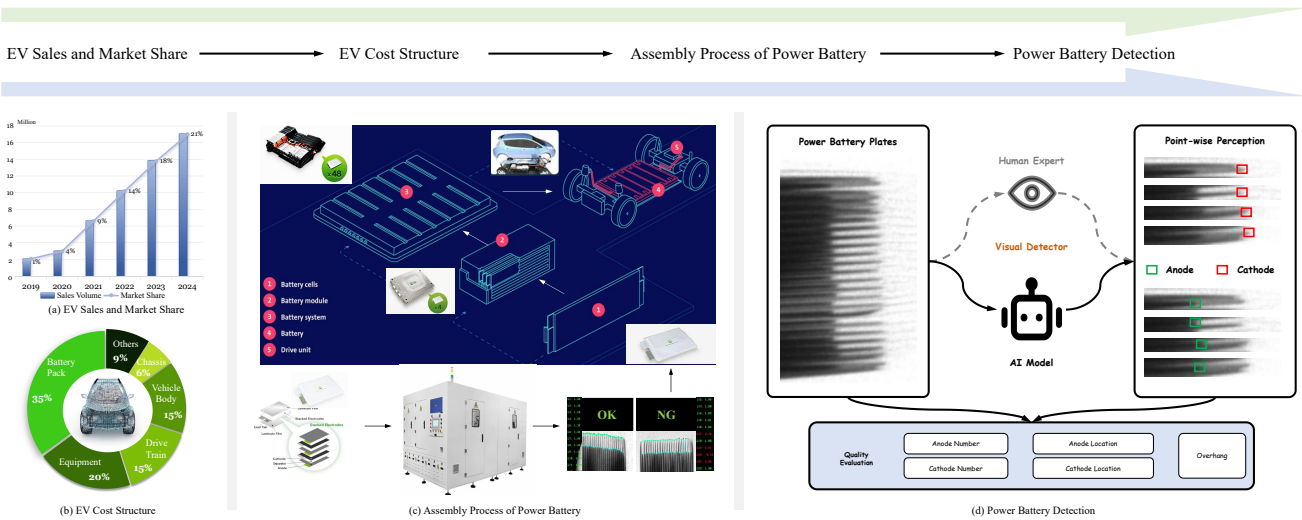


Fig. 1 Motivation of power battery detection (PBD). (a) EV sales are rapidly increasing, raising battery safety demands. (b) Battery packs account for $\sim 35\%$ of EV cost, highlighting their critical role. (c) Assembly process of power batteries for EVs, where PBD is applied to the battery cells before assembly. (d) Illustration of the power battery detection task.

ical economic and functional role. Ensuring its structural integrity requires reliable inspection throughout production. During cell assembly (Fig. 1(c)), hundreds of cathode and anode plates are stacked alternately. Any misalignment or overhang can lead to short circuits, overheating, or even explosion, creating serious safety risks. To address this, a post-assembly inspection process, termed power battery detection (PBD), is widely applied. As shown in Fig. 1(d), PBD uses X-ray images captured by digital radiography (DR) systems to localize cathode and anode endpoints with coordinate-level precision. This enables automatic computation of key quality indicators, such as the number of plates and their overhang¹, which determine whether a battery cell is acceptable (OK) or defective (No Good, NG). However, long-term manual inspections are subject to visual fatigue and human errors. Even top manufacturers relying on large re-inspection teams face high labor costs and limited efficiency.

Therefore, the development of an intelligent PBD model is an imminent need. To benchmark this new task, we first introduce PBD5K, the first large-scale power battery dataset with 5,000 X-ray images. It is constructed using an intelligent annotation pipeline that combines automatic filtering, model-assisted labeling, cross-validation, and hierarchical quality control, significantly improving labeling efficiency and accuracy. Compared with traditional visual tasks, PBD presents

¹ Number and overhang are two critical metrics in battery quality control. Number indicates the total count of anode/cathode plates, while overhang measures the average vertical offset between one anode and its adjacent cathodes.

Table 1 Attribute descriptions (see examples in Fig. 2(c)).

Attr	Description
P	<i>Pure Plate</i> . High-quality sample without any internal and external interference.
T	<i>Tilted Plate</i> . Deformation caused by excessively dense plates.
A	<i>Aberrant Plate</i> . 1) Plates visualization is incomplete due to occlusion. 2) Plates are not arranged in the order of anode \rightarrow cathode \rightarrow anode.
II	<i>Illumination Interference</i> . Visual thickness anomaly of the plate caused by deviations in the incident angle of the radiation source.
PI	<i>Plate Interference</i> . Other batteries blend into current view.
BI	<i>Bifurcation Interference</i> . A single plate produces a bifurcation.
TRI	<i>Tray Interference</i> . A battery tray is a device used for holding large battery packs in place. Close distance between the side plate and tray may cause visual interference.
TAI	<i>Tab Interference</i> . Battery tabs are the anode and cathode connectors that carry the cells' electrical current.
SI	<i>Separator Interference</i> . A battery separator is a type of polymeric membrane that is positioned between the anode and cathode.

several unique challenges: **I) Open Vision Problem Modeling**. Like emerging tasks such as character stroke extraction [38], insubstantial object detection [102], open vocabulary object detection and segmentation [16, 89], how to model a suitable AI-based solution is critical for the PBD task. **II) Single Pixel-Level Object Localization**. As shown in Fig. 2(a), PBD requires accurately identifying plate endpoints that are only one pixel in size among millions of pixels, and providing their precise coordinates. This level of search difficulty is akin to finding a needle in a haystack. **III) Multi-shot Imaging**. As shown in Fig. 2(b), X-ray imaging is conducted under various field-of-view settings, leading to significant variations in spatial resolution. Even under the same imaging setup, batteries may exhibit different physical dimensions or placement scales. **IV) Weak Feature Perception**. As clearly observed in Fig. 2(c), the plate endpoints exhibit extremely weak features and are visually similar to their surrounding regions. Especially under interference from bifurcated plates, separators, or trays, their visibility is further di-

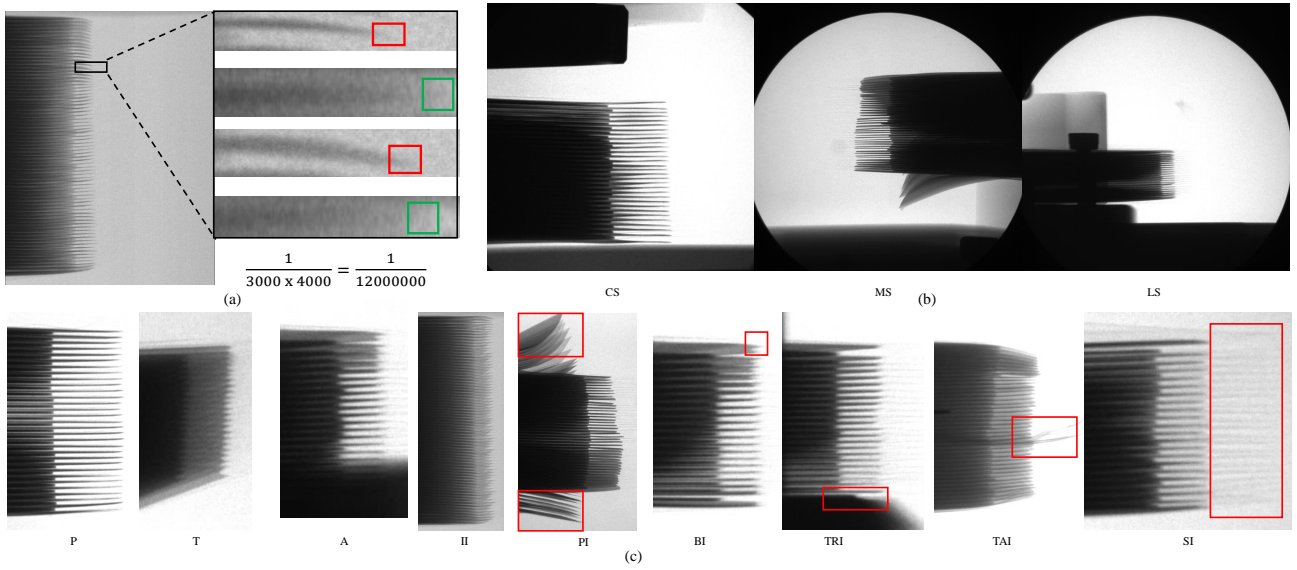


Fig. 2 Visual examples from the PBD5K dataset (best viewed zoomed in). (a) 1-pixel localization on high-resolution (3000×4000) X-ray images. (b) The imaging field-of-view include Close Shot (*CS*), Medium Shot (*MS*) and Long Shot (*LS*). (c) Examples of various attributes. See Tab. 1 for details.

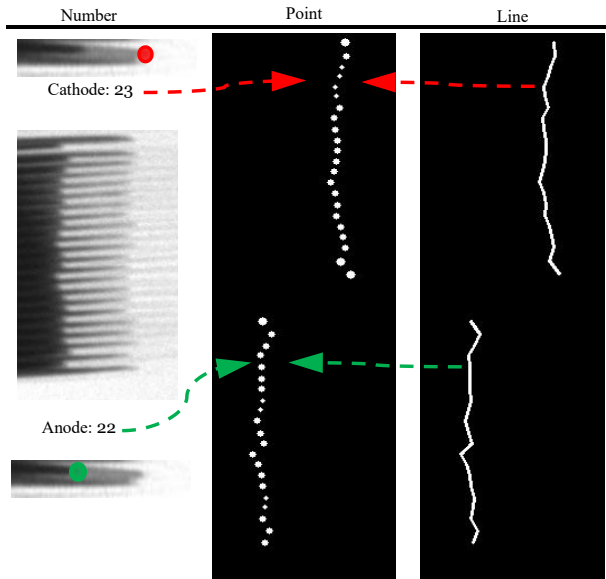


Fig. 3 Illustration of multi-clue mining with point, line and number clues.

minished. V) *Fine-grained Structural Semantics.*

PBD5K contains a wide range of overhang distribution patterns. When the distance between adjacent cathode and anode plates is small (less than 100 pixels), their visual appearances become easily confused. Since power batteries are manufactured with strict alternation between cathode and anode plates, accurate endpoint localization implicitly requires the model to understand the structural semantics, including the classification and ordering of electrode plates.

In this paper, we propose a multi-dimensional collaborative network for accurate PBD. Imitating the coarse-

to-fine human visual perception system [24,77], the model first perceives the battery region and then gradually refines the localization of each plate. Once the endpoints are precisely segmented, both their coordinates and total numbers can be derived. **First**, we reformulate PBD as a point-centric segmentation task, where the core objective is to predict a point map of single-pixel endpoints for cathode and anode plates. A U-shaped encoder-decoder [36,60] serves as the basic structure for point prediction. Inspired by multi-task learning [6,13,97] and the structural traits of power batteries, we introduce two auxiliary tasks: line segmentation and plate counting. As shown in Fig. 3, connecting predicted endpoints yields line maps that constrain spatial position and reduce ambiguity. Line supervision guides endpoint refinement, while the counting branch enforces consistency between the predicted and actual number of electrodes, mitigating false positives and omissions. By jointly learning from these three complementary clues, we establish a segmentation-centered multi-dimensional collaborative framework. **Next**, to improve localization under weak textures and noisy backgrounds, we utilize state space models (SSMs) [19–21, 42], which offer efficient long-range modeling with linear complexity. Compared to Transformer-based models [12, 43], SSMs are more suitable for high-resolution industrial images due to their lower computational cost. However, direct use of SSMs may amplify irrelevant large-region patterns (*e.g.*, trays or tabs), thereby overwhelming the subtle and sparse endpoint signals. To address this, we propose the prompt-filtered state space module (PF-SSM). It uses features from a representative prompt

image to generate dynamic filters that enhance plate features while suppressing distractors. Filtered features are then processed through a 2D Mamba block [42] for context modeling. This design improves robustness under low contrast, occlusion, or interference, directly addressing the challenges of *weak feature perception* and *fine-grained structural semantics*. **Third**, we embed the density-aware reordering state space module (DRSSM) at the tail of MDCNeXt to refine predictions in densely packed regions. General sequential scanning in SSM often mixes background and foreground features, fragmenting the already sparse electrode signals. This problem worsens in samples with densely packed plates, where spatial entanglement further weakens class-specific representations. DRSSM addresses this by using the coarse point map to semantically regroup features (e.g., cathode, anode, background) and reorder them into contiguous sequences. These reordered tokens are processed via state space modeling to enhance intra-class consistency. The refined features are then mapped back to their original layout, yielding sharper boundary localization and better category separation. **Last**, we design an adaptive label generation strategy for point segmentation. Specifically, we compute the spatial distance between adjacent homopolar plates based on annotations and use it as a reference radius to generate scale-aware ground truth masks. Unlike fixed-size masks, this adaptive mask better matches real spacing variations, improving robustness in both sparse and dense plate regions.

Our main contributions can be summarized as follows:

- We introduce power battery detection (PBD) as a new visual task in computer vision and construct the first benchmark dataset PBD5K, design an effective baseline, formulate comprehensive metrics, and explore label generation strategies to promote research on the PBD.
- We develop an efficient annotation pipeline for PBD5K that integrates automatic filtering, model-assisted pre-labeling, cross-validation, and multi-level quality control.
- We formulate PBD as a segmentation problem and propose MDCNeXt, a multi-dimensional collaborative framework that jointly leverages point, line, and number clues to improve both low-level details and high-level semantics.
- We successfully adapt state space modeling to MDCNeXt by introducing prompt filtering and density-aware reordering mechanisms, enabling its robust localization under weak representation and dense regions.

- We compare MDCNeXt with corner detection, crowd counting, general/tiny object detection and image segmentation methods. Extensive experiments demonstrate that the proposed MDCNeXt performs favorably against the state-of-the-art methods under different metrics.
- We provide systematic discussion and forward-looking outlook on some promising future directions for the PBD task, laying the foundation for long-term research and real-world deployment of automated battery quality inspection.

This paper is based on and extends our CVPR version [95] in the following aspects. I) We significantly expand the dataset from 1,500 to 5,000 images, forming a new benchmark PBD5K with richer variations in image resolution, plate number, overhang distribution and interference types, and provide a more detailed dataset analysis. II) An intelligent annotation pipeline is introduced to improve labeling efficiency and consistency, providing the industrial AI community with a transparent and reproducible workflow. III) We upgrade the MDCNet [95] to a stronger version named MDCNeXt by embedding the proposed prompt-filtered state space module and density-aware reordering state space module. IV) We conduct more extensive experiments, including quantitatively and qualitatively comparisons with generalist, general and specialized segmentation models in terms of ten metrics, showing consistent superiority of MDCNeXt. V) We provide a comprehensive introduction to related work, detailed implementation details, and thorough ablation studies. VI) We present an in-depth discussion on future directions of PBD, outlining promising research opportunities.

2 Related Work

2.1 Open Vision Problem Modeling

Emerging open vision problems often deviate from traditional tasks due to novel instance definitions, annotation challenges, or perceptual ambiguity, demanding tailored task abstraction and modeling. Liu *et al.* [38] formulate **Chinese character stroke extraction** as stroke-level instance segmentation, enabling fine-grained and transferable structural decomposition. Zhou *et al.* [102, 103] address the challenge of **insubstantial object detection** by treating faint or transparent targets as spatially diffuse regions with geometric uncertainty, and model detection through 3D voxel shift field estimation. Pang *et al.* [53] define **open-vocabulary camouflaged object segmentation** as a hybrid of open-set recognition and camouflage-aware segmentation, integrating vision-language priors and structural clues like

depth and edges to capture imperceptible objects. Chiu *et al.* [10] frame **wire segmentation** as a thin-structure semantic segmentation task under ultra-high-resolution constraints, emphasizing continuity-preserving modeling tailored for elongated, slender targets. Yang *et al.* [86] conceptualize **traffic sign interpretation** as a semantic reasoning task over interrelated signs, where the goal is to interpret visual signals into natural-language instructions through multi-level relational logic. Zhou *et al.* [101] tackle the **nighttime optical flow estimation** problem by casting it as cross-domain motion alignment, leveraging reflectance and gradient-aligned latent spaces to transfer motion priors from auxiliary domains under degraded visibility. Liu *et al.* [5] design **technical drawing parsing** as a vector-based structural graph learning problem, transforming CAD designs into spatial graphs where geometric primitives are modeled as relational nodes for precise topological inference. Wei *et al.* [80] further leverage a type-agnostic and expressive line-based representation of graphical primitives, instead of traditional point-based methods, enabling a unified abstraction that accommodates diverse elements in engineering and architectural diagrams.

These pioneering works show a common principle: solving underexplored visual problems starts with proper *task redefinition* and *representation design*, enabling meaningful perception and reasoning. Our work follows this line by introducing power battery detection as a new vision task, with a tailored representation and modeling strategy bridging real-world industrial needs and AI perception.

2.2 Object Detection, Counting and Segmentation

We introduce multiple potential modeling schemes for the PBD task and analyze related techniques.

Corner detection is widely used in motion detection, image matching, and video tracking. A corner point is typically defined as the intersection of two edges and can also be referred to as a feature point. Harris and Stephens [22] propose one of the earliest methods by directly computing the differential of the corner score with respect to direction. Shi–Tomasi [63] improves stability by selecting corners based on the minimum eigenvalue of the gradient matrix. Sub-pixel methods [7] further enhance accuracy by refining corner positions to real coordinates for geometric measurement or calibration. However, corner detectors are often not robust and typically require high redundancy to mitigate the impact of individual errors on recognition tasks.

Object detection aims to locate and classify semantic objects in images or videos. Many methods rely

on **bounding box prediction**, using rectangles to approximate object locations. Detectors are typically categorized into two paradigms: *I) Two-stage detectors*, such as Fast RCNN [17], Faster R-CNN [58], FPN [36], and RFCN [11], which generate region proposals before classification and refinement. *II) One-stage detectors*, such as RetinaNet [37], YOLOv10 [73], FCOS [69], and DETR [4], which directly predict bounding boxes and categories in a single forward pass. Although most single-stage methods have fast detection speed, they are usually not as accurate as the anchor-based two-stage detectors, especially in small objects. To bridge this gap, a number of **tiny object detection** methods have been developed to achieve a trade-off between accuracy and efficiency, including C3Det [34], CFNet [88], and HS-FPN [64].

Dense object counting task is to infer the number of objects in dense scenarios. Most CNNs-based methods [28, 54, 56, 74] predict a density map from a crowd image, where the summation of the density map is the crowd count. For the structures, some works are proposed to address scale variation [1, 28, 91], to refine the predicted density map [56, 62, 68], and to encode context information [66, 84]. For the loss function, L2 loss is usually used in many models but it is sensitive to the choice of variance in the Gaussian kernel [71]. Therefore, Bayesian loss [47] is proposed with point-wise supervision.

Image segmentation aims to simplify or transform an image into a more structured representation, facilitating further analysis. Diverse segmentation types exist in practice, including salient, camouflaged, transparent, and medical segmentation. Most methods [9, 51, 100] adopt a U-shaped encoder-decoder architecture [36, 60], where multi-level features are progressively fused to generate high-resolution masks. To enhance feature representation, some works [35, 93, 98, 107] incorporate attention mechanisms, such as spatial, channel-wise and gated attention to selectively emphasize informative clues. Meanwhile, handling scale variation among objects remains a key challenge. This has motivated research into multi-scale feature extraction techniques [8, 49, 87, 94, 99], including ASPP [8], Fold-ASPP [98], and DenseASPP [87], which aim to capture semantic clues across receptive fields of varying sizes. Recently, Transformer-based models [3, 67, 82] have attracted attention for their ability to model global context. Unlike CNNs with limited receptive fields, Transformers [70] utilize self-attention to capture long-range dependencies, improving performance in complex spatial tasks. Segformer [82] and SwinUNet [3] couple hierarchical encoding with attention-based decoding. However, their quadratic complexity and weak local bias limit scalability and fine-grained

prediction. In contrast, Mamba-based methods [72, 83] leverage selective state-space models to replace attention with structured recurrence, enabling linear time complexity and superior scalability. Mamba [19] excels in global dependency modeling with low memory cost and an inherent structural bias, suiting thin-structure or topology-aware tasks. Some hybrid CNN-Mamba models [39, 46] combine local detail preservation with global reasoning, and providing an efficient framework for high-resolution and real-time segmentation. With the growing pursuit of foundation models and artificial general intelligence, unified and generalist segmentation models are emerging to address diverse segmentation tasks with a single set of parameters. SAM [33] is trained on 1.1 billion masks, enabling high-quality segmentation with various prompts. UniverSeg [2] focuses on unifying medical image segmentation across diverse organs and modalities. SegGPT [76] offers flexible segmentation via visual in-context learning. HQSAM [29] improves SAM for high-resolution segmentation. SAM 2 [57] extends SAM to video by incorporating memory attention and multi-frame prompts. For complex context-dependent concepts, EVP [40] and GateNetv2 [99] integrate low-level structural prompts and gated context, while Spider [96] and VSCode [45] apply 2D prompt learning to model foreground-background relations. In this work, our proposed MDCNeXt integrates the aforementioned advanced techniques, including CNN-Mamba hybrid design, attention-based refinement, multi-scale modeling, and prompt-driven filtering, aiming to provide a high-precision segmentation for the PBD task.

2.3 Enhancing Weak Features in Complex Vision Tasks

In complex vision tasks, key targets often exhibit weak, sparse, or ambiguous features due to small object scales, low contrast, occlusion, vague boundaries, or background clutter. Such weak signals pose fundamental challenges in remote sensing, medical imaging and industrial inspection. To address this, recent studies enhance weak features via two main strategies: multi-modal and multi-structural clues fusion, both injecting complementary or contextual information into feature learning. Multi-modal fusion improves feature expressiveness by introducing multiple modalities. For example, Liu *et al.* [41] employ RGB-D for camouflaged object segmentation, Kim *et al.* [31] utilize RGB-T for transparent object segmentation, and Pang *et al.* [52] verify the complementarity between RGB-D and RGB-T modalities. Beyond visual signals, text serves as a strong auxiliary modality in semantically ambiguous scenes. CLIP [55] enable open-vocabulary recognition via large-scale image-text

pretraining, while Pang *et al.* [53] use textual descriptions to generalize camouflaged object segmentation to novel categories. In the medical domain, cross-modality fusion (*e.g.*, MRI, CT, PET) provides complementary anatomical and functional context for localizing subtle lesions [105]. Beyond modalities, structural priors such as edges, contours, and symmetry help delineate fuzzy or ambiguous targets. Edge-aware modules [15, 92, 106] guide fine-grained segmentation, while higher-level topological clues (*e.g.*, skeletons, geometric primitives) benefit tasks like polyp segmentation [78], shadow removal [25], and transparent object detection [81]. These structures isolate meaningful patterns amid visual noise. Our work aligns with this direction by constructing a multi-clue segmentation framework that jointly leverages point, line, and number clues to enhance weak feature perception, enabling robust object discovery in X-ray battery images with complex interference.

3 PBD5K Dataset

3.1 Image Collection and Annotation

The proposed PBD5K dataset is collected using the same DR device across over 10,000 power battery cells from 10 manufacturers, covering close, medium, and long shot views. To efficiently construct a high-quality industrial dataset, we design an intelligent annotation pipeline that integrates automated screening, uncertainty-guided active learning, and multi-expert quality control. The full workflow is illustrated in Fig. 4, where over 10,000 raw X-ray images are progressively filtered, annotated, and validated to form the final PBD5K benchmark with 5,000 images.

Automated Screening. The pipeline begins with the automated filtering of raw data. This stage includes battery integrity screening and duplicate image filtering. The former employs a lightweight object detection model to discard invalid samples with incomplete views (*e.g.*, batteries cut off at edges), overexposed images, and blank captures. The latter eliminates near-duplicate images by computing high-level visual similarity using pre-trained convolutional neural network (CNN) features. Specifically, each image is first encoded into a compact 512-dimensional representation using global average pooling over intermediate VGG [65] feature maps. To handle large-scale retrieval, we apply FAISS [27], a fast approximate nearest neighbor search library. Image pairs with Euclidean distance below a threshold are deemed duplicates. We then perform connected-component clustering on the similarity graph and retain one representative per cluster. This multi-stage screen-

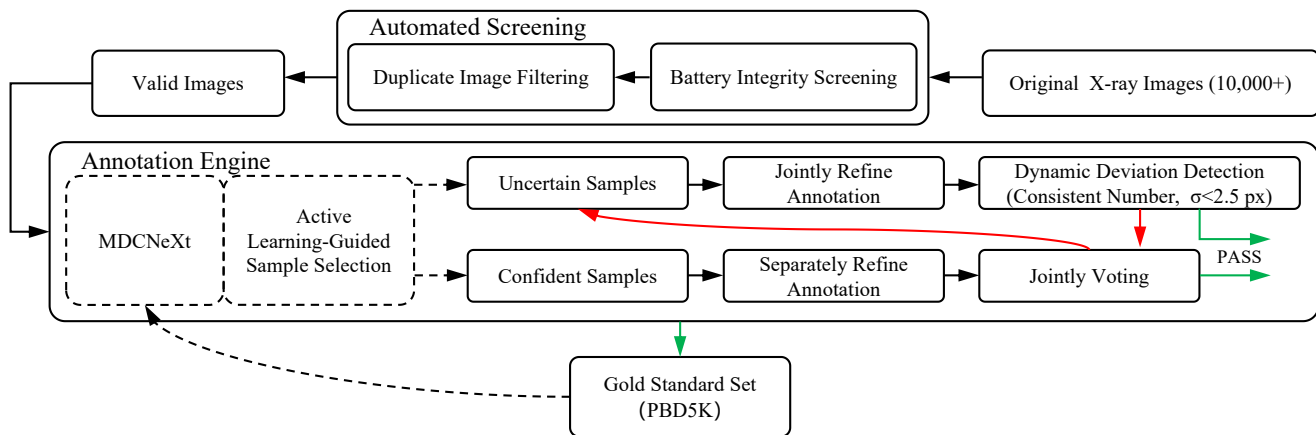


Fig. 4 The overall intelligent annotation pipeline with automated screening, annotation engine with active Learning, and multi-expert quality control. Red arrows (\rightarrow) indicate poor annotation quality, while green arrows (\rightarrow) indicate high-quality annotations that are included in the Gold Standard Set.

ing ensures the final dataset is both structurally complete and semantically diverse.

Annotation Engine with Active Learning. The annotation engine is driven by our MDCNeXt within an active learning loop. Initially, with no labeled samples, all valid images are sent to a multi-expert annotation stage. Each sample is independently labeled by three experts. A real-time deviation detection module checks consistency in point counts and spatial locations. If the annotations are consistent in number and have low position deviation, the system fuses them via coordinate averaging to form a gold standard. Otherwise, the sample proceeds to a voting stage with three additional experts to select the most plausible annotation. To avoid infinite review loops, we place constraints on voting depth. Once enough gold-standard labels are collected, MDCNeXt is trained and used to predict on unlabeled images. To assess the uncertainty of the coarse predictions, we evaluate the degree of binarization of the predicted maps. Specifically, we compute the difference between the maximum and minimum activation values of the sigmoid-activated map (ranging from 0 to 1). Based on this uncertainty estimation, the predicted samples are divided into two categories:

- **Uncertain Samples:** Predictions with a larger difference are routed back to the joint annotation pipeline, where multiple experts collaboratively review and revise the results.
- **Confident Samples:** Predictions with a lower difference are refined independently by individual experts. These refined annotations are then passed through the jointly voting stage for final validation and integration.

During the entire process, human expert teams work in parallel rather than sequentially, ensuring high through-

Table 2 Efficiency comparison between manual and intelligent annotation schemes.

Metric	Manual	Intelligent	Improvement
Average Annotation Time (min/image)	3.4	1.2	↑64.7%
Annotation Spatial Deviation (pixel)	3.5	0.9	↑74.3%
Proportion of Disputed Samples	22%	13%	↑40.9%
Rework Rate	17%	6%	↑64.7%

put. This active learning-driven annotation loop iteratively improves MDCNeXt and continues until convergence. Through this pipeline, we construct the PBD5K dataset, a gold-standard benchmark composed of 5,000 expertly annotated X-ray battery images, validated through automated and human-in-the-loop quality checks. As shown in Tab. 2, our approach significantly improves annotation efficiency and reliability compared to traditional manual schemes.

3.2 Dataset Analysis

Hierarchical Distribution of Categories and Attributes. As shown in Fig. 5, the collected images have 2 categories, 3 shots, 9 attributes and their proportions under each shot type are statistically reported in detail. Different battery types, manufacturing and packaging processes produce different thicknesses of batteries. Even if the DR device is calibrated, it still has different degrees of penetration for different thicknesses, thereby resulting in *Clear* and *Blur* X-ray images. The imaging field-of-view include close shot (*CS*), medium shot (*MS*) and long shot (*LS*). Each shot type further contains samples labeled with multiple common attributes: pure plate (**P**), tilted plate (**T**), aberrant plate (**A**), illumination interference (**II**), plate interference (**PI**), bifurcation interference (**BI**), tray interference (**TRI**),

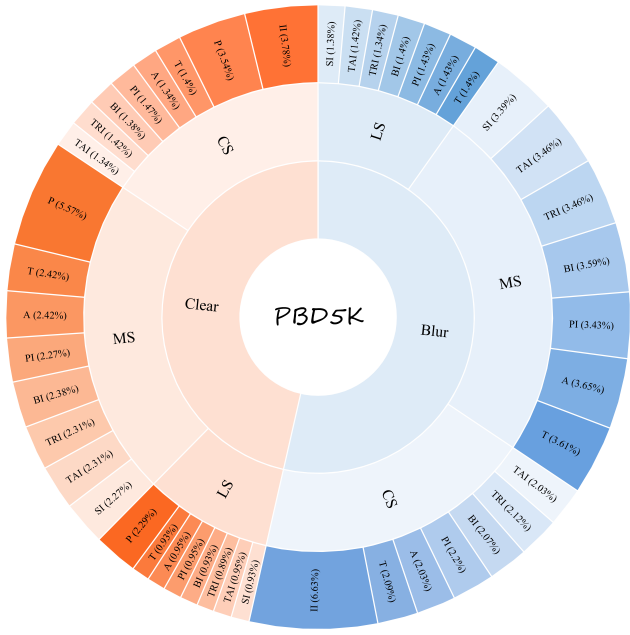


Fig. 5 Hierarchical distribution of categories, shots, and attribute types in the PBD5K dataset.

tab interference (**TAI**), and separator interference (**SI**). The quantitative proportions are marked beside each attribute. We can see that **P** only appears in the *Clear* category, **II** is exclusively found in the *CS* view, while **SI** does not occur in the *CS* view. The detailed definitions of these attributes are given in Tab. 1, and visual samples are presented in Fig. 2.

Co-Occurrence Distribution of Attributes. Fig. 6 (left) shows a dependency matrix where each value indicates the conditional probability of co-occurrence. The highly non-diagonal and asymmetric structure reveals complex inter-attribute relationships. **SI** frequently co-exists with many other attributes, acting as a common disturbance. In contrast, **TRI** and **TAI** rarely co-occur with others, indicating they are more isolated and category-specific attributes. Some combinations, such as **BI** + **PI** or **T** + **A**, occur frequently due to their correlation in battery production anomalies.

Multi-Dependency Relationships. In Fig. 6 (right), we provide a chord diagram to further visualize mutual dependencies. The arc thickness represents the degree of interaction between attributes. We can see that more than four attribute dependencies appear in all samples, which illustrates the diversity and complexity of this dataset.

Resolution, Overhang Distribution, and Plate Number. Fig. 7 presents three key structural features. (1) The dataset contains images of diverse resolutions, ranging from less than 200×200 to over 3000×3000

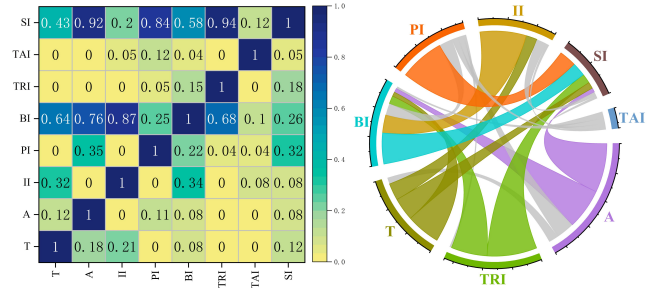


Fig. 6 Left: Co-occurrence distribution of attributes. The numbers in each grid indicate the proportion of images. Right: Multiple dependencies among these attributes. The larger the arc length, the higher the probability that one attribute is related to another.

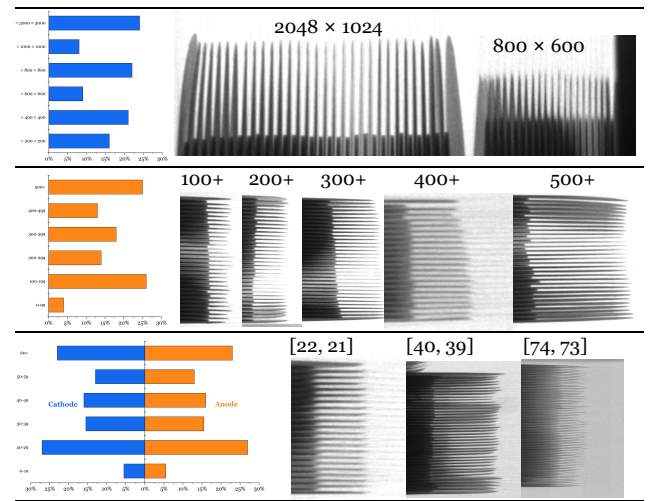


Fig. 7 Statistics and visualization of structural diversity in the PBD5K dataset, including image resolution, overhang and plate number distributions.

pixels. Representative examples (*e.g.*, 2048×1024 and 800×600) are visualized alongside the histogram. (2) We provide a statistical distribution of overhang values. Five examples with different overhang levels, demonstrating the wide range of structural inconsistencies. This variability is essential for evaluating model robustness to structural deviations. (3) The number of cathode/anode plates in each battery can be fewer than 20 or exceed 60. Three examples with different plate numbers clearly illustrate that increasing the number of plates poses significant challenges for visual plate disentanglement.

Dataset Splits. To ensure balanced coverage of various characteristics, we split the dataset into training and testing sets with a 6:4 ratio while maintaining distribution balance across categories, shots, and attributes. There are 3,000 images for training and 2,000 for testing. Furthermore, we split the test set into three

difficulty levels: regular (515 images), difficult (677 images), and tough (808 images), based on the degree of interference caused by different attributes and plate number.

3.3 Evaluation Metrics

According to the number and overhang criteria adopted by the manufacturers, we design eight complementary metrics to quantitatively evaluate the performance of algorithms. Specifically, they are number mean absolute error (AN-MAE, CN-MAE), number accuracy (AN-ACC, CN-ACC, PN-ACC) and position mean absolute error (AL-MAE, CL-MAE and OH-MAE) for the anode level, cathode level, and pair level, respectively. Let n_i^x and \hat{n}_i^x represent the predicted and ground truth plate numbers for the i -th image at level $x \in \{\text{anode, cathode, pair}\}$, and $p_{i,j}^y, \hat{p}_{i,j}^y$ represent the coordinates of the j -th plate at level $y \in \{\text{anode, cathode}\}$ for image i with resolution $H_i \times W_i$. The eight evaluation metrics are defined as follows:

$$\text{AN-MAE} = \frac{1}{N} \sum_{i=1}^N |n_i^{an} - \hat{n}_i^{an}|, \quad (1)$$

$$\text{CN-MAE} = \frac{1}{N} \sum_{i=1}^N |n_i^{ca} - \hat{n}_i^{ca}|, \quad (2)$$

$$\text{AN-ACC} = \frac{1}{N} \sum_{i=1}^N \mathbb{1}(n_i^{an} = \hat{n}_i^{an}), \quad (3)$$

$$\text{CN-ACC} = \frac{1}{N} \sum_{i=1}^N \mathbb{1}(n_i^{ca} = \hat{n}_i^{ca}), \quad (4)$$

$$\text{PN-ACC} = \frac{1}{N} \sum_{i=1}^N \mathbb{1}(n_i^{pair} = \hat{n}_i^{pair}), \quad (5)$$

$$\text{AL-MAE} = \frac{1}{N_p} \sum_{i=1}^N \frac{1}{n_i^{an}} \sum_{j=1}^{n_i^{an}} \frac{1}{H_i W_i} |p_{i,j}^{an} - \hat{p}_{i,j}^{an}|, \quad (6)$$

$$\text{CL-MAE} = \frac{1}{N_p} \sum_{i=1}^N \frac{1}{n_i^{ca}} \sum_{j=1}^{n_i^{ca}} \frac{1}{H_i W_i} |p_{i,j}^{ca} - \hat{p}_{i,j}^{ca}|, \quad (7)$$

$$\text{OH-MAE} = \frac{1}{N_p} \sum_{i=1}^N \frac{1}{n_i^{an}} \sum_{j=1}^{n_i^{an}} \frac{1}{H_i W_i} |o_{i,j} - \hat{o}_{i,j}|, \quad (8)$$

$$o_{i,j} = |p_{i,j}^{cathode} - p_{i,j}^{anode}| + |p_{i,j}^{cathode} - p_{i,j+1}^{anode}|, \quad (9)$$

where N is the total number of test samples and N_p is the number of samples with correctly predicted plate numbers. Note that, for an image, only when its number of AN or CN is predicted with 100% accuracy, we can further evaluate the corresponding position MAE. Coordinates must be sorted before calculating AL-MAE, CL-MAE and OH-MAE.

Generally, n_i^x can be obtained by counting the number of $p_{i,j}^y$. Corner detection directly predicts each endpoint's coordinates. General/Tiny object detection methods predict bounding boxes for endpoints, and we calculate the center coordinates of each box as $p_{i,j}^y$. Counting methods estimate n_i^x by summing predicted density maps. Segmentation-based methods produce point masks, from which $p_{i,j}^y$ is obtained by calculating the center coordinates for the circumscribed rectangle of each point map.

4 Proposed Framework

4.1 Overview

As shown in Fig. 8, the MDCNeXt adopts the encoder-decoder structure with a ResNet-50 [23] backbone. The encoder initially extracts five-level features, and the prompt and current pipelines share the same weights. The prompt-filtered state space module (PFSSM) uses the prompt features to filter out interfering information from the current features and generate pure plate appearance features. The point predictor outputs the coarse point segmentation map after passing through five decoder blocks. The line predictor and counting predictor assist in point prediction at the low-level detail and semantic levels, respectively. Finally, the density-aware reordering state space module (DRSSM) carefully refines the coarse point segmentation map and features to obtain a refined point map prediction.

4.2 Prompt-filtered State Space Module

As shown in Fig. 9, PFSSM consists of a prompt-based feature filter followed by a state space modeling block. It takes the feature map from the multi-scale feature encoder as input and outputs enhanced features for the point predictor. PFSSM aims to suppress irrelevant patterns (*e.g.*, trays, tabs, and bifurcations) while capturing long-range dependencies essential for accurate plate localization. We randomly choose a \mathbf{P} plate sample (see Fig. 2) as the prompt image. From the

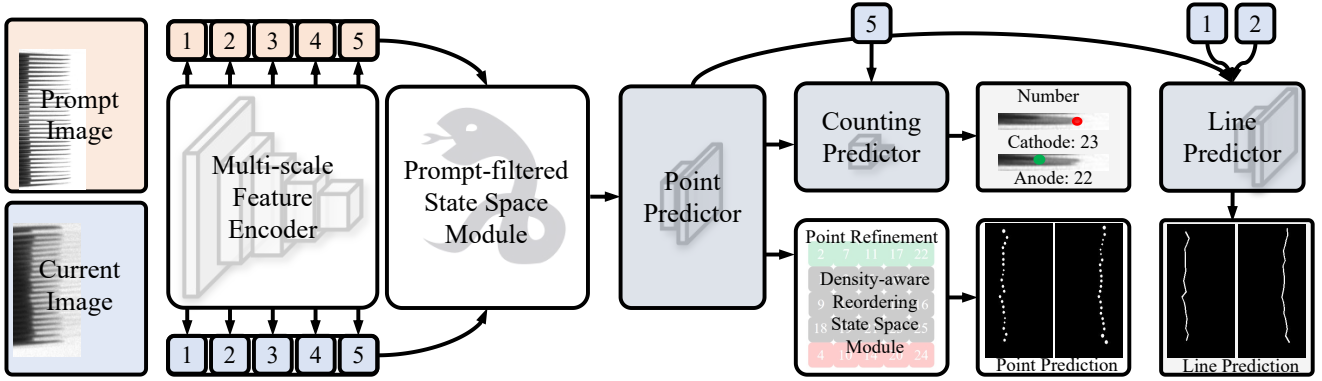


Fig. 8 Overview of our MDCNeXt framework. It adopts an encoder-decoder architecture with a shared ResNet-50 backbone to extract five-level features from both the prompt and current images. The prompt-filtered state space module (PFSSM) utilizes prompt features to remove interference from the current features, generating clean plate representations. The point predictor produces coarse segmentation maps through five decoding layers. The line and counting predictors serve as auxiliary branches to enhance point prediction at low-level detail and semantic levels, respectively. The density-aware reordering state space module (DRSSM) refines both features and coarse predictions to generate the final fine-grained point map.

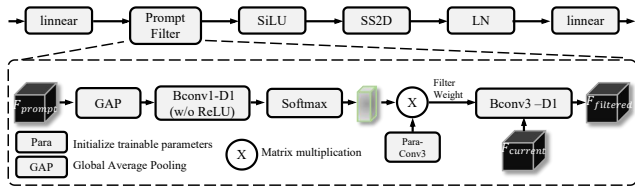


Fig. 9 Illustration of the prompt-filtered state space module. It takes multi-level current and prompt features as inputs.

prompt’s 1st–5th layer features, we extract multi-level information to construct dynamic filters. We take both the 5th prompt and current image features as an example to illustrate the process of prompt filtering. We first conduct global average pooling and convolution for F_{prompt} . Then, the softmax function distributes F_{prompt} with the channel-wise soft attention. Next, we initialize the 3×3 convolution with trainable parameters and multiply the soft attention to generate the aggregated parameters as the weights. The current feature map $F_{current}$ is then filtered by these weights using $Bconv3-D1$. The filtered features $F_{filtered}$ are passed through a $SiLU$ activation and a 2D Selective Scan (SS2D) [42]. SS2D performs to bridge 1D array scanning and 2D plane traversal, enabling the extension of selective SSMs to process vision data. This allows prompt information to be globally propagated throughout the current feature map in a content-aware and spatially aligned manner. Finally, the output is passed through layer normalization (LN) and a linear transformation to produce the final enhanced features. Overall, PFSSM serves as a prompt-driven enhancement module that both condenses high-level guidance from prompt features and es-

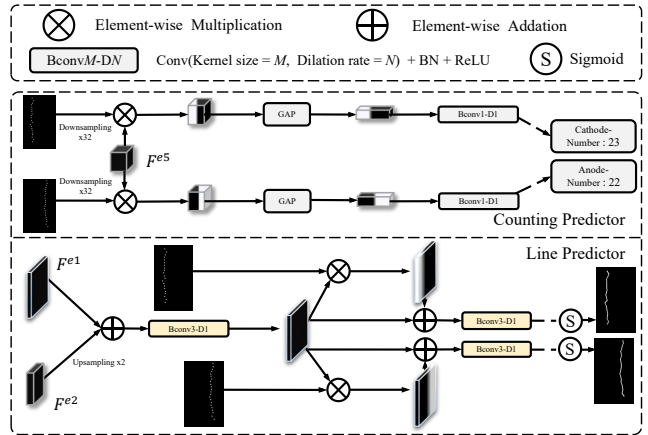


Fig. 10 Illustration of the counting predictor and line predictor. The former takes high-level features and predicted point maps as input to perform global plate number regression. The latter integrates low-level features and point predictions to produce line maps.

tablishes strong long-range dependencies between prompt and current images in an efficient manner.

4.3 Multi-Dimensional Decoder

Our multi-dimensional decoder consists of a point predictor, counting predictor, and line predictor. The point predictor adopts a general U-shaped architecture [36, 60], progressively fusing features output by each PFSSM to generate a coarse point map highly responsive to point locations. These coarse anode and cathode maps are subsequently used by both the counting and line predictors. As shown in Fig. 10, it illustrates counting predictor and line predictor.

• *Counting predictor.* The overall counting predictor is constructed to solve a regression problem. The inputs of the counting predictor are the high-level features ($F_{current}^{e5}$) and the predicted point maps (M_p^{anode} , $M_p^{cathode}$) of the anode and cathode plates from the point predictor. To narrow the search range of the counting objects, we utilize two predicted point maps as spatial attention to guide $F_{current}^{e5}$. The number of anode and cathode plates are computed as:

$$\begin{cases} N^{anode} = \text{ReLU}(\text{Conv}(\text{GAP}(\text{DS}(F_{current}^{e5}) \otimes M_p^{anode}))) \\ N^{cathode} = \text{ReLU}(\text{Conv}(\text{GAP}(\text{DS}(F_{current}^{e5}) \otimes M_p^{cathode}))) \end{cases}, \quad (10)$$

where $\text{DS}(\cdot)$ is downsampling, \otimes is element-wise multiplication, $\text{GAP}(\cdot)$ is global average pooling, and $\text{Conv}(\cdot)$ is a convolution layer with one-channel output. As an auxiliary task for the point segmentation, counting task can improve the query ability of high-level features on the number of plates at the global level, thereby enhancing the feature representation of the point branch.

• *Line predictor.* Generally speaking, detail information of contours often exists in the low-level features. Therefore, we build the line predictor with both low-level features ($F_{current}^{e1}$, $F_{current}^{e2}$) and the predicted point maps (M_p^{anode} , $M_p^{cathode}$) as inputs. We first aggregate the $F_{current}^{e1}$, $F_{current}^{e2}$ to generate the $F_{current}^{e1,2}$:

$$F_{current}^{e1,2} = \text{Conv}(F_{current}^{e1} + \text{US}(F_{current}^{e2})), \quad (11)$$

where $\text{US}(\cdot)$ is the upsampling operation. Next, $F_{current}^{e1,2}$ is separately computed with M_p^{anode} and $M_p^{cathode}$ in the form of residual [23] and predict line segmentation maps:

$$\begin{cases} L^{anode} = \text{S}(\text{Conv}(M_p^{anode} \otimes F_{current}^{e1,2}) + F_{current}^{e1,2}) \\ L^{cathode} = \text{S}(\text{Conv}(M_p^{cathode} \otimes F_{current}^{e1,2}) + F_{current}^{e1,2}) \end{cases}, \quad (12)$$

where $\text{S}(\cdot)$ is the element-wise sigmoid. As another auxiliary task of point segmentation, line segmentation can provide continuous segmentation clues to compensate and modify some plates that are not accurately predicted by point branch.

4.4 Density-aware Reordering State Space Module

As shown in Fig. 11, DRSSM takes the low-level feature and point map from the point predictor as input. First, the input is projected via a linear layer, followed by the depthwise separable convolution (DWConv) and SiLU activation. To prevent the foreground (anode/cathode) and background signals from being entangled during

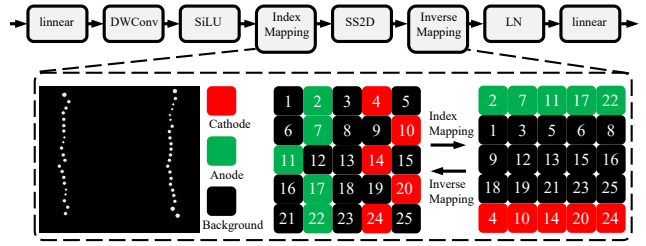


Fig. 11 Illustration of the density-aware reordering state space module. It takes low-level features and a coarse point map as inputs. Index mapping rearranges semantically similar pixels, and inverse mapping restores the original spatial layout after SS2D.

state space modeling, we introduce a density-aware reordering mechanism. Given the coarse point map $\hat{P} \in \mathbb{R}^{H \times W}$ predicted by the point predictor, we generate a pixel-wise semantic category index for each location (e.g., anode, cathode, background). We then flatten the input feature map $F \in \mathbb{R}^{H \times W \times C}$ and reorder it into a new sequence $F_{reordered} \in \mathbb{R}^{N \times C}$ by grouping pixels of the same semantic label together. This rearrangement brings semantically similar features closer, facilitating more coherent long-range dependency modeling. The SS2D performs selective scanning over the reordered sequence, enhancing intra-class consistency while suppressing inter-class interference. After processing the reordered sequence $F_{reordered}$ using the SS2D, we restore the original 2D layout by performing the inverse operation of the previously applied index mapping. Specifically, we use the saved semantic index to reposition each token back to its original spatial location, reconstructing the feature map $F_{refined} \in \mathbb{R}^{H \times W \times C}$. The refined output is normalized by a LN and projected through another linear layer. The final result is a refined point-wise segmentation map with improved plate boundary discrimination.

4.5 Label Generation and Supervision

For point segmentation, a direct strategy of generating the ground truth of point mask is to use circular regions of the same radius for each plate. As shown in the 1st - 3rd columns of Fig. 12, the point masks are yielded under the radius of 1, 3, and 5 pixels, respectively. It can be seen that the fixed radius often produces very dense or sparse point masks for different types of batteries, which increases the difficulty of point segmentation. To this end, we design a novel distance-adaptive label generation strategy. It computes the diameter of each point according to the distance of adjacent plates. As shown in the 4th - 6th columns of Fig. 12, the point masks are generated under the diameter of $0.1x$, $0.3x$,

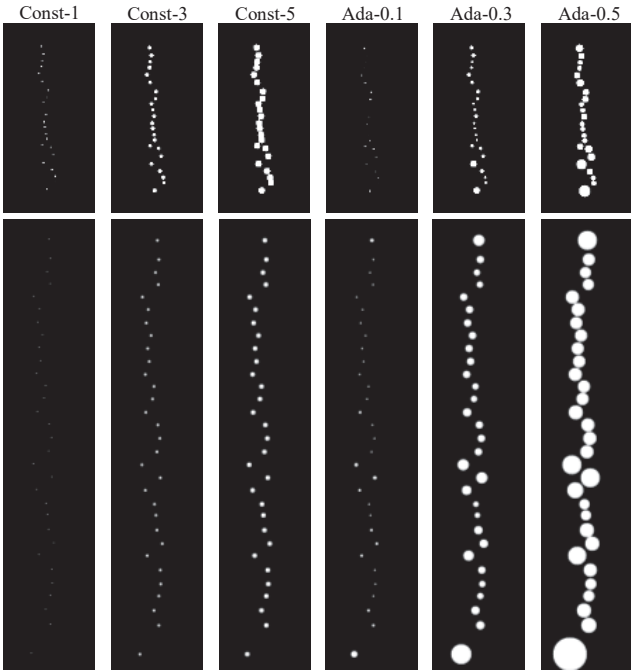


Fig. 12 Visualization of the ground-truth point masks under different strategies for point label generation.

and $0.5x$ distance, respectively. The labels of counting and line segmentation can be separately obtained by the connected component analysis and connecting each endpoint in the point mask in sequence. For the point and line segmentation predictors, we use the weighted IoU loss and binary cross entropy (BCE) loss, which have been widely adopted in segmentation tasks. We use the same definitions as in [14, 79, 100, 104]. For the counting predictor, we adopt the common L1 loss. The total training loss is written as follows:

$$\mathcal{L}_{\text{total}} = \lambda_1 \cdot \mathcal{L}_{\text{point}}^{\text{refine}} + \lambda_2 \cdot \mathcal{L}_{\text{point}}^{\text{coarse}} + \lambda_3 \cdot \mathcal{L}_{\text{count}} + \lambda_4 \cdot \mathcal{L}_{\text{line}}, \quad (13)$$

where $\lambda_1, \lambda_2, \lambda_3, \lambda_4$ are balancing weights, empirically set to $\lambda_1 = \lambda_2 = 1$, $\lambda_3 = 0.05$, and $\lambda_4 = 0.5$. Point segmentation receives the highest weights as it is our core task, while count loss is down-weighted to avoid dominating early optimization due to its large magnitude.

5 Experiments

5.1 Implementation Details

Our MDCNeXt model is implemented in PyTorch and trained on 4 NVIDIA Tesla V100 GPUs for 150 epochs with a batch size of 4. All X-ray images are resized

to 512×512 . We adopt the Adam optimizer [32] with $\beta_1 = 0.5$, $\beta_2 = 0.999$. The initial learning rate is set to 1×10^{-4} . To stabilize training, we apply a weight decay of 1×10^{-3} and gradient clipping with a threshold of 0.5. A step-wise learning rate decay schedule reduces the learning rate by 0.9 every 120 epochs. To improve generalization, we apply data augmentation techniques including random horizontal flipping, multi-scale resizing ($0.75\times$, $1.0\times$, $1.25\times$), and random brightness adjustment. To prevent the model from overfitting to a specific prompt during inference, we adopt a prompt randomization strategy throughout training. Instead of using a fixed prompt sample, each training epoch randomly selects a pure plate from the training set to serve as the prompt input. This approach encourages the model to learn robust prompt-invariant representations.

5.2 Comparison with Corner Detection, Crowd Counting, General and Tiny Object Detection Solutions

Quantitative Comparison. As shown in Tab. 3, we conduct a comprehensive comparison across various representative methods that serve as potential solutions to the PBD task. The evaluation spans regular, difficult, and tough splits, and we further report the average scores across them. The key observations are as follows: *I*) Our segmentation-based MDCNeXt and MDCNet achieve state-of-the-art performance across different splits under all metrics. It confirms that modeling the PBD task as a visual point segmentation problem is a correct solution. Moreover, MDCNeXt further outperforms MDCNet with average gains exceeding 18%, 17%, and 20% on AN-ACC, CN-ACC, and PN-ACC, respectively. *II*) The complementarity among different evaluation metrics highlights the necessity of using a multi-metric evaluation scheme for PBD. For example, tiny object detection methods have AN-MAE and CN-MAE scores close to ours (within 2 units) on the regular split. However, their AN-ACC and CN-ACC drop by more than 20% compared to MDCNeXt. Besides, the OH-MAE metric may fail to capture systematic shifts. When both AN and CN position predictions are slightly displaced in the same direction, OH-MAE might still appear low. In the tough split, other methods show AL-MAE and CL-MAE scores that are more than twice their OH-MAE, exposing serious localization issues. Therefore, combining multiple metrics gives a more reliable and precise evaluation. This is consistent with the strict spatial accuracy requirements of the PBD task, where even small errors are magnified and

Table 3 Quantitative comparison of different methods. \uparrow and \downarrow indicate that the larger scores and the smaller ones are better, respectively. The best scores are highlighted in **red**. “—” represents that the results are not available because these methods can not provide coordinate information or their prediction accuracy of the number of plates is zero. “Average” refers to the average scores across the Regular, Difficult, and Tough test splits.

Dataset	Metrics	Corner Detection			Crowd Counting			General/Tiny Object Detection					Segmentation	
		Harris [22]	Shi-tomasi [63]	Sub-pixel [7]	BL [47]	CUT [54]	IOCFomer [68]	RetinaNet [37]	DETR [4]	YOLOv10 [73]	CFINet [34]	HS-FPN [64]	MDCNet CVPR 2024 [95]	MDCNeXt (Ours)
Regular	AN-MAE \downarrow	195.2021	121.4027	165.5050	3.8430	2.9021	2.3879	2.1290	3.2294	2.7320	1.9377	1.3402	0.3028	0.2175 \uparrow 28%
	CN-MAE \downarrow	4892.2022	239.3201	219.2020	3.1252	2.3026	2.0352	1.9346	5.3212	4.3824	1.3798	1.1202	0.2187	0.1320 \uparrow 40%
	AN-ACC \uparrow	0.0000	0.0000	0.0000	0.4892	0.5324	0.4512	0.6483	0.5186	0.6232	0.6825	0.7024	0.8932	0.9379 \uparrow 5%
	CN-ACC \uparrow	0.0000	0.0000	0.0000	0.5112	0.5512	0.4732	0.6626	0.4984	0.5465	0.6942	0.7360	0.8964	0.9456 \uparrow 5%
	PN-ACC \uparrow	0.0000	0.0000	0.0000	0.4673	0.4956	0.4072	0.6135	0.4215	0.4576	0.6356	0.6735	0.8531	0.9165 \uparrow 7%
	AL-MAE \downarrow	—	—	—	—	—	—	4.5640	8.5600	3.4985	2.4745	2.3475	1.3245	1.1537 \uparrow 13%
	CL-MAE \downarrow	—	—	—	—	—	—	4.7754	7.9456	3.0782	2.3750	2.1576	1.3948	1.2234 \uparrow 12%
	OH-MAE \downarrow	—	—	—	—	—	—	3.9432	8.2468	2.9670	2.4150	2.3756	1.3750	1.0102 \uparrow 27%
Difficult	AN-MAE \downarrow	136.7474	84.1242	115.5250	1.7576	2.6755	1.4256	1.7576	2.8465	2.0789	2.8645	1.3974	0.4732	0.3515 \uparrow 26%
	CN-MAE \downarrow	4218.2002	178.1542	245.0121	1.8546	3.0250	1.6251	1.7450	3.0856	2.0227	2.9875	1.3746	0.4450	0.3428 \uparrow 23%
	AN-ACC \uparrow	0.0000	0.0000	0.0000	0.3986	0.2578	0.3659	0.4745	0.3145	0.4576	0.5175	0.5846	0.8078	0.8973 \uparrow 11%
	CN-ACC \uparrow	0.0000	0.0000	0.0000	0.2546	0.1974	0.4745	0.3610	0.3091	0.3420	0.4010	0.4715	0.7746	0.8552 \uparrow 10%
	PN-ACC \uparrow	0.0000	0.0000	0.0000	0.2847	0.1127	0.2461	0.2587	0.2545	0.2475	0.2978	0.3726	0.6988	0.7983 \uparrow 14%
	AL-MAE \downarrow	—	—	—	—	—	—	10.2643	31.4544	9.1798	8.9599	8.4756	4.1547	1.3702 \uparrow 67%
	CL-MAE \downarrow	—	—	—	—	—	—	10.9875	34.7055	9.3256	8.8750	8.2745	4.0025	1.2953 \uparrow 68%
	OH-MAE \downarrow	—	—	—	—	—	—	6.0875	12.2540	7.2560	7.1515	7.4250	3.9846	1.1603 \uparrow 71%
Tough	AN-MAE \downarrow	275.4540	165.1059	190.0571	3.5425	2.9546	2.8472	7.1502	12.3564	8.7600	7.4658	6.9875	4.2547	0.7873 \uparrow 81%
	CN-MAE \downarrow	4750.1010	225.0325	295.3512	2.1978	2.1785	3.0201	6.3572	9.0971	11.1015	7.1150	6.0220	3.1042	0.3781 \uparrow 88%
	AN-ACC \uparrow	0.0000	0.0000	0.0000	0.2512	0.3741	0.3075	0.1912	0.0975	0.2541	0.2987	0.3105	0.5402	0.7873 \uparrow 46%
	CN-ACC \uparrow	0.0000	0.0000	0.0000	0.2843	0.2915	0.4253	0.3102	0.1423	0.1967	0.2547	0.3746	0.5015	0.7341 \uparrow 46%
	PN-ACC \uparrow	0.0000	0.0000	0.0000	0.2034	0.2545	0.2275	0.1340	0.0672	0.0975	0.1440	0.2116	0.4125	0.6263 \uparrow 52%
	AL-MAE \downarrow	—	—	—	—	—	—	17.8345	48.2451	20.0240	14.3545	17.1545	8.3425	1.2145 \uparrow 85%
	CL-MAE \downarrow	—	—	—	—	—	—	20.9871	54.0202	22.1544	16.2540	14.8741	7.5471	0.9826 \uparrow 87%
	OH-MAE \downarrow	—	—	—	—	—	—	7.0470	18.9345	8.1574	9.0202	8.1345	5.3451	0.9979 \uparrow 81%
Average	AN-MAE \downarrow	198.7517	121.1357	153.6240	2.8988	2.8283	2.1546	3.6786	6.1642	4.5086	4.1834	3.2749	1.7094	0.4645 \uparrow 73%
	CN-MAE \downarrow	4571.8041	209.7727	255.4058	2.2980	2.5524	2.2029	3.3551	5.6962	5.7035	3.9707	2.8822	1.2869	0.3005 \uparrow 77%
	AN-ACC \uparrow	0.0000	0.0000	0.0000	0.3720	0.3679	0.3681	0.4234	0.2936	0.4314	0.4859	0.5222	0.7392	0.8705 \uparrow 18%
	CN-ACC \uparrow	0.0000	0.0000	0.0000	0.3307	0.3204	0.4575	0.4215	0.3014	0.3455	0.4270	0.5068	0.7135	0.8375 \uparrow 17%
	PN-ACC \uparrow	0.0000	0.0000	0.0000	0.3042	0.2593	0.2813	0.3079	0.2341	0.2508	0.3327	0.3956	0.6416	0.7705 \uparrow 20%
	AL-MAE \downarrow	—	—	—	—	—	—	11.3590	31.2427	11.3876	9.1160	9.8354	4.8435	1.2617 \uparrow 74%
	CL-MAE \downarrow	—	—	—	—	—	—	12.7727	34.3529	12.0594	9.6990	8.9334	4.5309	1.1709 \uparrow 74%
	OH-MAE \downarrow	—	—	—	—	—	—	5.8601	13.4835	6.4567	6.5644	6.3649	3.7732	1.0667 \uparrow 72%

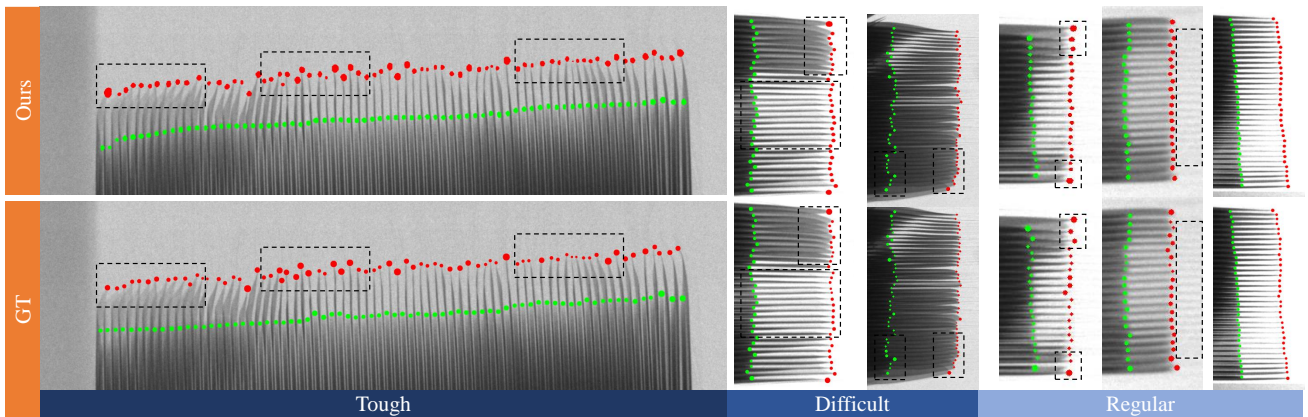


Fig. 13 Qualitative results on regular, difficult, and tough examples with varying attributes, resolutions, overhang levels, and numbers of plates. Black dashed boxes ([-]) highlight the challenging regions. Best viewed zoomed in.

“almost correct” results are not acceptable. *III*) MDCNeXt shows strong robustness and stability across all splits. Its AL-/CL-MAE values fluctuate within only 0.3. In contrast, other object detection methods suffer from significant accuracy degradation as the number of plates sheets increases and the accumulation of inter-

ference types. In the tough split, their AL-MAE and CL-MAE scores exceed 15, reflecting a strong decline in positional precision compared to the regular split.

Qualitative Comparison. Fig. 13 presents visual predictions of MDCNeXt across diverse battery configurations. Tough sample is a high-resolution image with

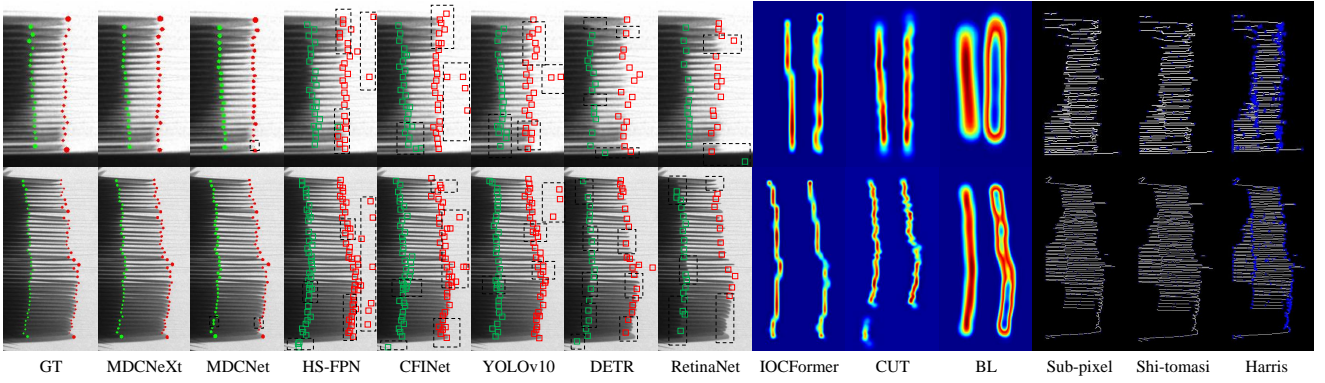


Fig. 14 Visual comparison with other general/tiny object detection-based [4, 37, 64, 73, 88], counting-based [47, 54, 68], corner detection-based [7, 22, 63] solutions. We directly visualize the predicted results (Ours: Segmentation map, General/Tiny object detection methods: Bounding box, Counting methods: Density map, Corner detection methods: Corner map) without any post-processing operations. Black dashed boxes ([-]) highlight the regions with obvious prediction failures. Best viewed zoomed in.

Table 4 Quantitative comparison of image segmentation methods. All ten metrics are widely used across various segmentation branches [14, 49, 82, 96], with details introduced in the survey [99]. \uparrow and \downarrow indicate that higher and lower values are better, respectively. Best scores are highlighted in **red**. MDCNeXt’s relative improvements over MDCNet are highlighted in **green**. “Average” denotes the mean scores across Regular, Difficult, and Tough test splits. For prompt-based generalist models (*i.e.*, SAM 2 and SegGPT), we use the same pure battery images and their corresponding masks as those in MDCNeXt as prompts to generate predictions for the test set.

Dataset	Method	Pub.	Backbone	$PA \uparrow$	$F_{\beta}^{max} \uparrow$	$F_{\beta}^{mean} \uparrow$	$F_{\beta}^{\omega} \uparrow$	$S_m \uparrow$	$E_m \uparrow$	$mIoU \uparrow$	$mDice \uparrow$	$BER \downarrow$	$\mathcal{M} \downarrow$
Regular	SAM 2 [57]	ICLR 2025	Hiera-B+ [61]	0.9802	0.2473	0.2213	0.1979	0.5932	0.7026	0.5121	0.2722	0.3541	0.0177
	SegGPT [76]	ICCV 2023	ViT-L [12]	0.9818	0.2163	0.1958	0.1932	0.5541	0.7319	0.5551	0.1958	0.3880	0.0182
	DeepLabV3+ [9]	ECCV 2018	ResNet-101 [23]	0.9867	0.5078	0.4278	0.4106	0.6438	0.9124	0.5920	0.4379	0.2711	0.0147
	SegFormer [82]	NeurIPS 2021	MiT-B5 [82]	0.9848	0.5435	0.4326	0.4020	0.6726	0.9074	0.6020	0.4541	0.2820	0.0134
	Spider [96]	ICML 2024	ConvNeXt-L [44]	0.9888	0.6425	0.5970	0.6212	0.7836	0.9425	0.6820	0.6278	0.1422	0.0097
	ZoomNeXt [50]	TPAMI 2024	ResNet-50 [23]	0.9888	0.6320	0.6073	0.6320	0.7825	0.9617	0.6923	0.6342	0.1302	0.0092
	MDCNet [95]	CVPR 2024	ResNet-50 [23]	0.9909	0.6730	0.6635	0.7083	0.7912	0.9687	0.7432	0.7023	0.1107	0.0081
	MDCNeXt	-	ResNet-50 [23]	0.9924	0.6979	0.6971	0.7337	0.8113	0.9786	0.7857	0.7248	0.1101	0.0076
			$\uparrow 0.2\%$	$\uparrow 3.7\%$	$\uparrow 5.1\%$	$\uparrow 3.6\%$	$\uparrow 2.5\%$	$\uparrow 1.0\%$	$\uparrow 5.7\%$	$\uparrow 3.2\%$	$\uparrow 0.5\%$	$\uparrow 6.2\%$	
Difficult	SAM 2 [57]	ICLR 2025	Hiera-B+ [61]	0.9836	0.1989	0.1782	0.1678	0.5029	0.7302	0.5780	0.1011	0.4474	0.0187
	SegGPT [76]	ICCV 2023	ViT-L [12]	0.9817	0.1499	0.1359	0.1337	0.5281	0.6867	0.5335	0.1347	0.4233	0.0182
	DeepLabV3+ [9]	ECCV 2018	ResNet-101 [23]	0.9865	0.3691	0.3742	0.3542	0.4109	0.9102	0.5532	0.3801	0.3080	0.0142
	SegFormer [82]	NeurIPS 2021	MiT-B5 [82]	0.9888	0.3390	0.3512	0.3210	0.3902	0.8921	0.5721	0.3670	0.3303	0.0153
	Spider [96]	ICML 2024	ConvNeXt-L [44]	0.9900	0.4412	0.4740	0.4412	0.6021	0.9314	0.6023	0.4921	0.2344	0.0129
	ZoomNeXt [50]	TPAMI 2024	ResNet-50 [23]	0.9888	0.5012	0.5079	0.4936	0.6785	0.9508	0.6289	0.5182	0.2161	0.0117
	MDCNet [95]	CVPR 2024	ResNet-50 [23]	0.9908	0.5652	0.5420	0.5372	0.7084	0.9538	0.6709	0.5690	0.1761	0.0094
	MDCNeXt	-	ResNet-50 [23]	0.9913	0.6252	0.6245	0.6611	0.7726	0.9758	0.7459	0.6522	0.1461	0.0086
			$\uparrow 0.1\%$	$\uparrow 10.6\%$	$\uparrow 15.2\%$	$\uparrow 23.1\%$	$\uparrow 9.1\%$	$\uparrow 2.3\%$	$\uparrow 11.2\%$	$\uparrow 14.6\%$	$\uparrow 17.0\%$	$\uparrow 8.5\%$	
Tough	SAM 2 [57]	ICLR 2025	Hiera-B+ [61]	0.9840	0.1312	0.1102	0.0981	0.4980	0.7022	0.5320	0.0921	0.4467	0.0186
	SegGPT [76]	ICCV 2023	ViT-L [12]	0.9819	0.0914	0.0824	0.0776	0.5092	0.6022	0.5158	0.0790	0.4579	0.0180
	DeepLabV3+ [9]	ECCV 2018	ResNet-101 [23]	0.9878	0.2712	0.1997	0.1939	0.2892	0.7920	0.3702	0.3083	0.3999	0.0178
	SegFormer [82]	NeurIPS 2021	MiT-B5 [82]	0.9890	0.2521	0.2001	0.2032	0.2782	0.7808	0.3840	0.3012	0.3911	0.0173
	Spider [96]	ICML 2024	ConvNeXt-L [44]	0.9896	0.3831	0.3221	0.3353	0.4483	0.9312	0.5201	0.4032	0.2411	0.0146
	ZoomNeXt [50]	TPAMI 2024	ResNet-50 [23]	0.9888	0.4378	0.3792	0.3511	0.5189	0.9433	0.5811	0.4732	0.2235	0.0129
	MDCNet [95]	CVPR 2024	ResNet-50 [23]	0.9890	0.4735	0.4012	0.3832	0.5733	0.9511	0.6021	0.5034	0.2190	0.0121
	MDCNeXt	-	ResNet-50 [23]	0.9903	0.5641	0.5633	0.5793	0.7353	0.9745	0.7153	0.5872	0.1831	0.0097
			$\uparrow 0.1\%$	$\uparrow 19.1\%$	$\uparrow 40.4\%$	$\uparrow 51.2\%$	$\uparrow 28.3\%$	$\uparrow 2.5\%$	$\uparrow 18.8\%$	$\uparrow 16.6\%$	$\uparrow 16.4\%$	$\uparrow 19.8\%$	
Average	SAM 2 [57]	ICLR 2025	Hiera-B+ [61]	0.9829	0.1884	0.1663	0.1520	0.5245	0.7136	0.5455	0.1421	0.4231	0.0184
	SegGPT [76]	ICCV 2023	ViT-L [12]	0.9818	0.1472	0.1332	0.1300	0.5284	0.6697	0.5331	0.1316	0.4259	0.0181
	DeepLabV3+ [9]	ECCV 2018	ResNet-101 [23]	0.9870	0.3717	0.3289	0.3145	0.4297	0.8708	0.5012	0.3707	0.3296	0.0155
	SegFormer [82]	NeurIPS 2021	MiT-B5 [82]	0.9878	0.3622	0.3210	0.3020	0.4250	0.8584	0.5161	0.3672	0.3384	0.0155
	Spider [96]	ICML 2024	ConvNeXt-L [44]	0.9896	0.4734	0.4543	0.4517	0.5968	0.9342	0.5950	0.4970	0.2129	0.0127
	ZoomNeXt [50]	TPAMI 2024	ResNet-50 [23]	0.9888	0.5134	0.4899	0.4810	0.6513	0.9511	0.6290	0.5328	0.1965	0.0115
	MDCNet [95]	CVPR 2024	ResNet-50 [23]	0.9902	0.5619	0.5256	0.5291	0.6840	0.9567	0.6662	0.5811	0.1738	0.0100
	MDCNeXt	-	ResNet-50 [23]	0.9912	0.6232	0.6225	0.6521	0.7699	0.9761	0.7458	0.6489	0.1494	0.0087
			$\uparrow 0.1\%$	$\uparrow 10.9\%$	$\uparrow 18.4\%$	$\uparrow 23.2\%$	$\uparrow 12.6\%$	$\uparrow 2.0\%$	$\uparrow 11.9\%$	$\uparrow 11.7\%$	$\uparrow 14.3\%$	$\uparrow 13.0\%$	

over 70 plate layers, where dense stacking, fine-scale structures, and boundary fluctuations make the task

highly challenging. Difficult samples involve the large overhang, illumination interference, and tightly packed

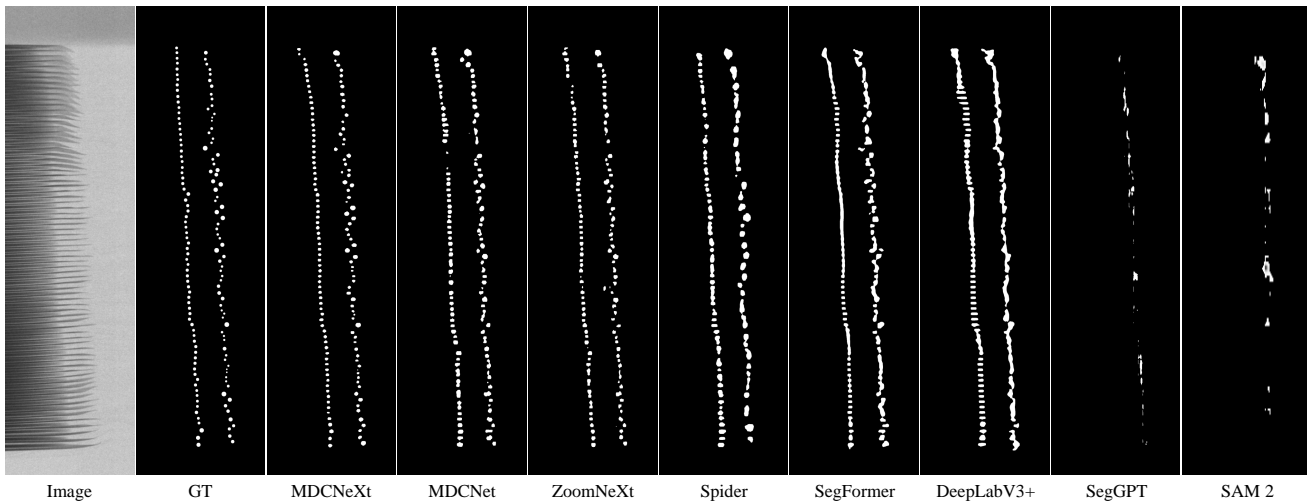


Fig. 15 Visual comparison with different image segmentation methods on binarized point maps for both anode and cathode.

distributions. Regular samples present bifurcation interference, separator interference and pure plate structures. In all these scenarios, MDCNeXt achieves consistently precise and robust predictions. Fig. 14 shows visual comparisons with other methods. MDCNet produces prediction errors at the endpoints when facing bifurcation interference and shows adhesion issues in dense regions. Box-based detection methods (HS-FPN, CFNet, YOLOv10) fail under bifurcations, trays, and separators, often producing redundant boxes prediction. DETR and RetinaNet are unable to overcome illumination interference, leading to many missed detections. Counting methods provide rough density maps but cannot localize each plate individually. Corner detection methods will yield redundant point maps and can not distinguish plate endpoints from general intersection points even if we have performed edge extraction to pre-filter a large amount of background irrelevant to plate endpoints.

5.3 Comparison with Image Segmentation Methods

Quantitative Comparison. To comprehensively evaluate MDCNeXt’s segmentation performance, we compare it with generalist models (SAM 2 [57], SegGPT [76]), general segmentation frameworks (DeepLabV3+ [9], SegFormer [82]), and context-dependent concept segmentation models (Spider [96], ZoomNeXt [50]). As shown in Table 4, ten widely adopted segmentation metrics are used for evaluation. From the average scores, SAM 2 and SegGPT perform reasonably on PA and S_m due to the dominance of background regions and structure-aware properties, but underperform on other metrics. This suggests that these in-context learning-based mod-

Table 5 Efficiency comparison of different segmentation methods in terms of parameter size and computational cost. The best two results are highlighted in **red** and **green**, respectively. The worst results are marked with underline.

Metrics	SAM 2 [57]	SegGPT [76]	DeepLabV3+ [9]	SegFormer [82]	Spider [96]	ZoomNeXt [50]	MDCNet [95]	MDCNeXt (Ours)
Parameters (MB)↓	216.40	370.26	58.94	84.75	<u>394.21</u>	28.46	49.54	41.54
GFLOPs↓	128.40	<u>655.65</u>	121.54	372.52	171.42	150.02	27.62	73.16

els struggle to propagate prompt features into the main segmentation branch for fine-grained guidance, limiting their adaptability to tasks like PBD even with large-scale pretraining. In contrast, Spider and ZoomNeXt benefit from foreground-background comparison and rich-scale fusion, outperforming general segmentation methods. Notably, MDCNeXt achieves the best results across all metrics. On the tough split, it surpasses MDCNet with improvements of 51.2% in F_β^w , 18.8% in $mIoU$, and 19.8% in \mathcal{M} , showing the effectiveness of our prompt-filtered and density-aware reordering state space modules. Tab. 5 further presents the efficiency comparison. MDCNeXt still shows clear advantages, achieving a good balance between parameter size and computation.

Qualitative Comparison. Fig. 15 shows the qualitative results on a tough sample. MDCNeXt outputs points with sizes and spacing aligned to local variations, showing high consistency with the ground truth. MDCNet and ZoomNeXt show point adhesions and discontinuities, while Spider suffers from merging multiple adjacent points into large responses. SegFormer and DeepLabV3+ fail to localize individual points, generating line-like outputs. SegGPT and SAM 2 barely capture plate structures, resulting in poor predictions. Overall, the visualization highlights the comprehensive capa-

Table 6 Ablation experiments of each component in the MDCNeXt.

Dataset	Method	AN-MAE _L	CN-MAE _L	AN-ACC _↑	CN-ACC _↑	PN-ACC _↑	AL-MAE _L	CL-MAE _L	OH-MAE _L
Regular	Baseline	2.3821	2.0212	0.7023	0.7320	0.6792	2.0321	2.1623	2.4392
	+ CP	1.5320	1.5012	0.7911	0.7932	0.7509	2.1023	2.1123	2.4086
	+ LP	1.1021	1.0023	0.8212	0.8412	0.8032	1.5320	1.4762	1.5633
	+ Prompt Stream	0.5077	0.5632	0.8744	0.8664	0.8398	1.5402	1.4402	1.5222
	+ PFSSM	0.2288	0.1794	0.9132	0.9230	0.8746	1.2722	1.3021	1.0432
+ DRSSM	0.2175	0.1320	0.9379	0.9456	0.9165	1.1537	1.2234	1.0102	
Difficult	Baseline	2.7982	2.6200	0.5021	0.4922	0.4132	7.1211	7.1069	5.3988
	+ CP	1.9921	1.8902	0.5794	0.5633	0.5090	7.0232	7.2109	5.0231
	+ LP	1.7032	1.5022	0.6211	0.6420	0.5543	5.0330	5.1211	3.0232
	+ Prompt Stream	0.8973	0.9012	0.7342	0.7212	0.6532	4.4547	4.7034	3.3203
	+ PFSSM	0.4299	0.4023	0.8302	0.8023	0.7232	2.2320	2.5460	1.7721
+ DRSSM	0.3515	0.3428	0.8973	0.8552	0.7983	1.3702	1.2953	1.1603	
Tough	Baseline	8.2110	7.5456	0.3105	0.3526	0.2075	13.4512	12.0812	6.4516
	+ CP	6.7008	6.4545	0.3750	0.4100	0.2575	12.2545	12.9697	6.8510
	+ LP	6.3907	6.0762	0.4178	0.4405	0.3028	10.2010	9.1250	6.3444
	+ Prompt Stream	5.3210	4.5456	0.4500	0.4846	0.3912	9.1425	7.9450	5.9450
	+ PFSSM	2.1021	1.5012	0.6502	0.6271	0.5299	3.4544	2.0877	1.8946
+ DRSSM	0.7873	0.3781	0.7873	0.7341	0.6263	1.2145	0.9826	0.9979	
Average	Baseline	4.5233	4.1331	0.4888	0.5067	0.4121	7.9534	7.5175	4.9931
	+ CP	3.4675	3.3350	0.5647	0.5706	0.4862	7.5269	7.8474	4.9686
	+ LP	3.1351	2.9218	0.6038	0.6251	0.5333	5.8809	5.5384	3.7715
	+ Prompt Stream	2.2944	2.0478	0.6944	0.6785	0.5290	4.9604	3.7458	3.1527
	+ PFSSM	0.9442	0.7169	0.7906	0.7741	0.6968	2.3986	2.0706	1.6259
+ DRSSM	0.4645	0.3005	0.8705	0.8375	0.7705	1.2617	1.1709	1.0667	

Table 7 Ablation experiments of state space modeling, prompt filter and reordering operation in PFSSM and DRSSM. M1: w/o SSM in PSSM. M2: w/o prompt filter in PSSM. M3: w/o reordering operation in DRSSM. M4: replace DRSSM with multiple convolution layers.

Dataset	Method	AN-MAE _L	CN-MAE _L	AN-ACC _↑	CN-ACC _↑	PN-ACC _↑	AL-MAE _L	CL-MAE _L	OH-MAE _L
Regular	Baseline	2.3821	2.0212	0.7023	0.7320	0.6792	2.0321	2.1623	2.4392
	MDCNeXt	0.2175	0.1320	0.9379	0.9456	0.9165	1.1537	1.2234	1.0102
	M1	0.2475	0.1812	0.9109	0.9120	0.8956	1.2032	1.2445	1.0138
	M2	0.2511	0.1942	0.9002	0.9020	0.8848	1.2205	1.3214	1.0836
	M3	0.2298	0.1777	0.9103	0.9204	0.8702	1.2790	1.3056	1.1890
M4	0.2260	0.1780	0.9121	0.9205	0.8764	1.2571	1.3126	1.0733	
Difficult	Baseline	2.7982	2.6200	0.5021	0.4922	0.4132	7.1211	7.1069	5.3988
	MDCNeXt	0.3515	0.3428	0.8973	0.8552	0.7983	1.3702	1.2953	1.1603
	M1	0.4896	0.4288	0.8025	0.8123	0.7436	1.7325	1.3646	1.2754
	M2	0.5346	0.5794	0.8213	0.7787	0.7097	2.0252	2.0711	1.4546
	M3	0.3954	0.3841	0.8371	0.8021	0.7152	2.0984	2.0715	1.4635
M4	0.3947	0.3754	0.8507	0.8211	0.7325	2.0741	2.2150	1.2513	
Tough	Baseline	8.2110	7.5456	0.3105	0.3526	0.2075	13.4512	12.0812	6.4516
	MDCNeXt	0.7873	0.3781	0.7873	0.7341	0.6263	1.2145	0.9826	0.9979
	M1	1.8411	1.0215	0.7092	0.6630	0.5416	2.0211	1.4516	1.0321
	M2	2.1641	1.5123	0.6315	0.6406	0.5219	2.2154	1.5145	1.2541
	M3	2.1765	1.7121	0.6741	0.6451	0.5468	3.0976	2.1545	1.0812
M4	2.0084	1.5401	0.6513	0.6289	0.5316	3.0790	2.1450	1.2015	
Average	Baseline	4.5233	4.1331	0.4888	0.5067	0.4121	7.9534	7.5175	4.9931
	MDCNeXt	0.4645	0.3005	0.8705	0.8375	0.7705	1.2617	1.1709	1.0667
	M1	0.8847	0.5657	0.7988	0.7874	0.7144	1.6939	1.3631	1.1257
	M2	1.0132	0.7960	0.7774	0.7637	0.6912	1.8824	1.6896	1.2912
	M3	0.9557	0.7805	0.8008	0.7794	0.6981	2.2256	1.9024	1.2634
M4	0.8975	0.7188	0.7990	0.7816	0.7015	2.2039	1.9589	1.1886	

bility of each model in handling scale variation, spatial precision, and feature discrimination.

5.4 Ablation Study

Each Component. We analyze the contribution of each component in Tab. 6. Our baseline is a point segmentation branch built on FPN [36] with a ResNet-50 backbone. First, we can see that the baseline has been able to outperform most competitors except HS-FPN, validating the suitability of point-based segmentation for the PBD task. Next, we add the counting predictor (CP) and line predictor (LP) to further refine the point segmentation at both high-level and low-level features. The former improves the accuracy of plate counting, while the latter helps adjust the positioning errors. Thus, multi-dimensional features complement each other and improve overall performance.

Table 8 Quantitative comparison of different label generation strategies and settings for the point segmentation branch. Const-1/3/5 refers to masks with radius of 1/3/5 pixels. The results are averaged across the three test set splits.

Method	AN-MAE _L	CN-MAE _L	AN-ACC _↑	CN-ACC _↑	PN-ACC _↑	AL-MAE _L	CL-MAE _L	OH-MAE _L
Const-1	6.8215	7.3420	0.3215	0.3334	0.2014	14.2512	11.0842	6.0204
Const-3	3.1415	3.0510	0.5712	0.5413	0.4896	6.1522	5.1545	2.9451
Const-5	3.3611	3.0026	0.5901	0.5874	0.5211	5.0215	4.9436	3.8421
Ada-0.1	3.0720	2.9496	0.6282	0.5746	0.5344	4.2012	4.7315	3.6762
Ada-0.3	0.4645	0.3005	0.8705	0.8375	0.7705	1.2617	1.1709	1.0667
Ada-0.5	1.7434	1.1553	0.7326	0.7251	0.6314	2.2015	2.0214	1.5141

Table 9 Stability evaluation of MDCNeXt with randomly selected prompt inputs.

No.	AN-MAE _L	CN-MAE _L	AN-ACC _↑	CN-ACC _↑	PN-ACC _↑	AL-MAE _L	CL-MAE _L	OH-MAE _L
1	0.4645	0.3005	0.8705	0.8375	0.7705	1.2617	1.1709	1.0667
2	0.4645	0.3005	0.8705	0.8375	0.7705	1.2617	1.1709	1.0667
3	0.4645	0.3005	0.8705	0.8375	0.7705	1.2617	1.1709	1.0667
4	0.4645	0.3005	0.8705	0.8375	0.7705	1.2617	1.1709	1.0667
5	0.4645	0.3005	0.8705	0.8375	0.7705	1.2617	1.1709	1.0667

Table 10 Quantitative comparison between joint and separate training for anode and cathode plates.

Method	AN-MAE _L	CN-MAE _L	AN-ACC _↑	CN-ACC _↑	PN-ACC _↑	AL-MAE _L	CL-MAE _L	OH-MAE _L
Joint Training	0.4645	0.3005	0.8705	0.8375	0.7705	1.2617	1.1709	1.0667
Separate Training	0.4898	0.3321	0.8604	0.8012	0.7626	1.2812	1.1692	1.1032

Then, we incorporate the prompt stream to guide the current image stream with pure plate features through simple convolution fusion. This addition provides consistent improvements across all splits under different metrics. Finally, we introduce the state-space modeling into the architecture. PFSSM is integrated into the multi-level feature fusion between current and prompt streams. From the average results, we observe that “+ PFSSM” shows consistent improvements compared to “+ Prompt Stream” with the gain of 14% and 57% in terms of PN-ACC and OH-MAE. DRSSM is added at the tail of the framework to further refine the point maps. On the tough split, PN-ACC increases from 0.5299 to 0.6263, and AL/CL-MAE is reduced by more than 50%.

Effectiveness of State Space Modeling, Prompt Filter and Reordering Operation. As shown in Tab. 7, we evaluate four variants of MDCNeXt. First, removing the state space modeling in PFSSM (M1) leads to significant performance degradation. Compared to the full MDCNeXt, the average AN-MAE and CN-MAE worsen from 0.4645 and 0.3005 to 0.8847 and 0.5657, while AN-ACC and CN-ACC drop from 0.8705 and 0.8375 to 0.7874 and 0.7144, respectively. These results confirm the critical role of SSM in modeling contextual relationships between the current and prompt streams. Next, removing the prompt filter in PFSSM (M2) leads to a notable performance decline. The average PN-ACC drops from 0.7705 to 0.7062, while OH-MAE deteriorates from 1.0667 to 1.2912. These results indicate that the prompt filter is essential for refining

the prompt signal and suppressing irrelevant interference. Then, we verify the effectiveness of the reordering operation by removing it in DRSSM (M3) and replacing DRSSM with multiple convolutional layers (M4). We can see that both modifications lead to consistent performance drops. Thus, simply stacking more convolutional layers cannot match the performance of the proposed reordering-based refinement. Finally, the gap between M3 and M4 suggests that directly applying SSM without the reordering mechanism in the final refinement stage loses its density-aware advantage, even underperforming vanilla convolution.

Label Generation Strategies. For point segmentation, we conduct a series of experiments about label generation strategies as discussed in Sec. 4.5. As shown in Tab. 8, the model trained under the Ada-0.3 performs best in terms of number accuracy and localization error among all the six settings. The distance-adaptive strategy consistently outperforms the constant strategy.

Selection of Prompts. In Tab. 9, we evaluate the performance of the model using five different groups of \mathbf{P} attribute images as the prompt input. It can be seen that MDCNeXt shows strong stability and generalization without dependence on a specific prompt. Thus, the strategy of random selection during training indeed makes MDCNeXt robust against different prompts when testing.

Joint Training vs. Separate Training. Joint training refers to using a single unified model to simultaneously generate predictions related to both anode and cathode plates in a single training process, whereas separate training involves two independent models. Due to the use of a single set of parameters and a joint training process, a mutual learning mechanism can be established between anode and cathode, which helps enhance the model’s discriminative ability and prevents confusion between the two plate types caused by the short overhang. As shown in Tab. 10, the jointly trained model achieves superior performance while using only half the parameters compared to the separate training setting.

6 Future Works and Outlook

This paper establishes a benchmark dataset and baseline for instance-level plate detection in power battery X-ray imagery. Despite promising results, many research directions and community challenges remain open for future exploration.

I) Toward High-precision Segmentation and Unified Clue Modeling. Our extensive experiments show that segmentation precision is strongly correlated

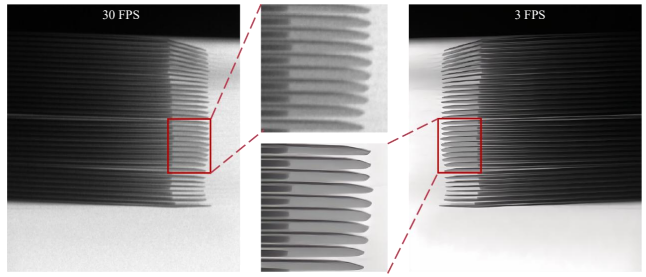


Fig. 16 Comparison of X-ray image quality at 30 FPS and 3 FPS exposure times.

with detection accuracy, especially on tough samples. Thus, highly accurate segmentation will remain a key research focus. Beyond segmentation quality, holistic strategies that incorporate complementary clues such as bounding boxes, geometric layouts, and topological structures remain underexplored. For example, bounding boxes are more robust to overlap and adhesion, while segmentation excels at spatial localization. A promising direction is to design unified frameworks that fuse the strengths of both representations via selection, reweighting, or joint optimization.

II) Blind Image Enhancement under Domain Constraints. As shown in Fig. 16, X-ray image clarity is highly sensitive to exposure time and acquisition parameters. Physical techniques such as prolonged exposure, multi-frame stacking, increased X-ray dosage, and high-sensitivity detectors can significantly reduce blur and ghosting, enhancing fine structural contrast. However, these approaches often face with practical limitations, including increased acquisition time, manual intervention, and high tuning costs, making them unsuitable for real-time industrial settings. To address these challenges, we advocate for domain-aware blind enhancement techniques. We can leverage multi-domain adaptive transfer learning and hybrid-domain unsupervised strategies to integrate natural image denoising or super-resolution priors with real PBD data. Once high-quality blind enhancement is achieved, different production lines will no longer be constrained by harsh imaging conditions and the need for extensive manual calibration.

III) Fine-grained Industrial Image Generation. High-quality and diverse battery data is essential for building robust foundation models in PBD. On the one hand, collecting real X-ray samples from different manufacturers is a long-term effort. On the other hand, we believe that generating targeted synthetic data based on specific interference attributes serves as an important complement, offering significant performance gains for PBD before sufficient real data is available. How-

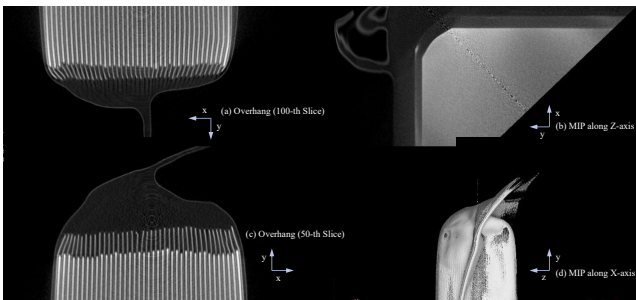


Fig. 17 Visualization of industrial CT data for battery inspection, including slice views and MIP images along different axes.

ever, most general-purpose generative models [59, 90] are designed for natural scenes and focus on global content realism, lacking control over intricate local structures, such as individual defects or subtle texture changes. In the future, we plan to develop a controllable fine-grained generation framework tailored to industrial scenarios. Based on end-to-end training with industrial data, the focus will be on achieving pixel-level generation conditioned on interference types and spatial layouts, rather than merely ensuring local and global semantic consistency.

IV) Lifelong and Rapid Incremental Adaptation. Battery product iterations in industry often occur at a weekly or even faster pace, requiring detection models to quickly adapt to new specifications with minimal performance degradation for old classes. Thus, it is critical to develop lifelong learning and incremental adaptation strategies that support fast tuning with minimal labeled data, while avoiding catastrophic forgetting.

V) High-speed and High-precision Industrial CT Reconstruction. As shown in Fig. 17, we visualize some industrial CT data, including slice views for overhang inspection (a, c) and maximum intensity projection (MIP) images along different axes (b: Z-axis, d: X-axis) for metal inclusions or microcracks. Compared with 2D X-ray imaging, volumetric CT provides more comprehensive structural insights, making it valuable for full-scope battery inspection. We plan to extend the PBD dataset into a 3D version by incorporating CT scans, which will significantly enhance the detection of internal quality issues. However, achieving real-time, high-resolution ($>3K$) CT reconstruction under industrial constraints remains highly challenging. Recent advances like 3D gaussian splatting (GS) [30] have shown promise in surface-level reconstruction using multi-view inputs [18, 75]. Future research may explore hybrid neural-physical frameworks that incorporate CT physical projection models and 3D GS repre-

sentations to enable end-to-end CT reconstruction from arbitrary views. In this process, sparse-view sampling, coarse-to-fine refinement pipelines, and the deployment of customized CUDA-based implementations can help accelerate the reconstruction speed.

7 Conclusion

We have presented the first comprehensive study on power battery detection (PBD) from complex industrial X-ray imagery. Specifically, we build a complex PBD5K dataset, formulate evaluation metrics and develop a segmentation-based multi-dimensional collaborative framework (*i.e.*, MDCNeXt). Compared with many potential modeling solutions and cutting-edge segmentation methods, our MDCNeXt demonstrates better performance under different metrics and shows strong robustness in tough samples with dense plates and structural interference. The above contributions offer the community an opportunity to design new models for the PBD task. In the future, we plan to extend PBD5K to 3D CT data and encourage research on domain-aware blind image enhancement, fine-grained industrial image generation, and high-speed and high-precision industrial CT reconstruction, toward more reliable full-scope battery inspection.

Data availability statement: All datasets used and studied in this paper are publicly available. The source code and datasets are publicly available at PBD5K.

References

1. D. Babu Sam, S. Surya, and R. Venkatesh Babu. Switching convolutional neural network for crowd counting. In *CVPR*, pages 5744–5752, 2017.
2. V. I. Butoi, J. J. G. Ortiz, T. Ma, M. R. Sabuncu, J. Guttag, and A. V. Dalca. Universeg: Universal medical image segmentation. In *ICCV*, pages 21438–21451, 2023.
3. H. Cao, Y. Wang, J. Chen, D. Jiang, X. Zhang, Q. Tian, and M. Wang. Swin-unet: Unet-like pure transformer for medical image segmentation. In *ECCV*, pages 205–218, 2022.
4. N. Carion, F. Massa, G. Synnaeve, N. Usunier, A. Kirillov, and S. Zagoruyko. End-to-end object detection with transformers. In *ECCV*, pages 213–229, 2020.
5. A. Carrara, S. Nousias, and A. Borrmann. Vectorgraph-net: Graph attention networks for accurate segmentation of complex technical drawings. *arXiv preprint arXiv:2410.01336*, 2024.
6. R. Caruana. Multitask learning: A knowledge-based source of inductive bias. In *ICML*, pages 41–48, 1993.
7. D. Chen and G. Zhang. A new sub-pixel detector for x-corners in camera calibration targets. In *International Conference in Central Europe on Computer Graphics and Visualization*, 2005.

8. L.-C. Chen, G. Papandreou, I. Kokkinos, K. Murphy, and A. L. Yuille. Deeplab: Semantic image segmentation with deep convolutional nets, atrous convolution, and fully connected crfs. *IEEE TPAMI*, 40:834–848, 2017.
9. L.-C. Chen, Y. Zhu, G. Papandreou, F. Schroff, and H. Adam. Encoder-decoder with atrous separable convolution for semantic image segmentation. In *ECCV*, pages 801–818, 2018.
10. M. T. Chiu, X. Zhang, Z. Wei, Y. Zhou, E. Shechtman, C. Barnes, Z. Lin, F. Kainz, S. Amirghodsi, and H. Shi. Automatic high resolution wire segmentation and removal. In *CVPR*, pages 2183–2192, 2023.
11. J. Dai, Y. Li, K. He, and J. Sun. R-fcn: Object detection via region-based fully convolutional networks. In *NeurIPS*, 2016.
12. A. Dosovitskiy, L. Beyer, A. Kolesnikov, D. Weissenborn, X. Zhai, T. Unterthiner, M. Dehghani, M. Minderer, G. Heigold, S. Gelly, et al. An image is worth 16x16 words: Transformers for image recognition at scale. In *ICLR*, 2021.
13. L. Duong, T. Cohn, S. Bird, and P. Cook. Low resource dependency parsing: Cross-lingual parameter sharing in a neural network parser. In *ACL*, pages 845–850, 2015.
14. D.-P. Fan, G.-P. Ji, T. Zhou, G. Chen, H. Fu, J. Shen, and L. Shao. Pranet: Parallel reverse attention network for polyp segmentation. In *MICCAI*, pages 263–273, 2020.
15. D.-P. Fan, T. Zhou, G.-P. Ji, Y. Zhou, G. Chen, H. Fu, J. Shen, and L. Shao. Inf-net: Automatic covid-19 lung infection segmentation from ct images. 39(8):2626–2637, 2020.
16. G. Ghiasi, X. Gu, Y. Cui, and T.-Y. Lin. Scaling open-vocabulary image segmentation with image-level labels. In *ECCV*, pages 540–557. Springer, 2022.
17. R. Girshick. Fast r-cnn. In *ICCV*, pages 1440–1448, 2015.
18. H. Go, B. Park, J. Jang, J.-Y. Kim, S. Kwon, and C. Kim. Splatflow: Multi-view rectified flow model for 3d gaussian splatting synthesis. In *CVPR*, pages 21524–21536, 2025.
19. A. Gu and T. Dao. Mamba: Linear-time sequence modeling with selective state spaces. In *COLM*, 2024.
20. A. Gu, K. Goel, and C. Ré. Efficiently modeling long sequences with structured state spaces. In *ICLR*, 2022.
21. A. Gu, I. Johnson, K. Goel, K. Saab, T. Dao, A. Rudra, and C. Ré. Combining recurrent, convolutional, and continuous-time models with linear state space layers. *NeurIPS*, 34:572–585, 2021.
22. C. Harris, M. Stephens, et al. A combined corner and edge detector. In *Alvey vision conference*, number 50, pages 10–5244, 1988.
23. K. He, X. Zhang, S. Ren, and J. Sun. Deep residual learning for image recognition. In *CVPR*, pages 770–778, 2016.
24. J. Hegdé. Time course of visual perception: coarse-to-fine processing and beyond. *Progress in neurobiology*, 84(4):405–439, 2008.
25. X. Hu, C.-W. Fu, L. Zhu, J. Qin, and P.-A. Heng. Direction-aware spatial context features for shadow detection and removal. 42(11):2795–2808, 2019.
26. International Energy Agency. Global ev outlook 2024, 2024. Accessed: 2025-06-11.
27. J. Johnson, M. Douze, and H. Jégou. Billion-scale similarity search with gpus. *IEEE Transactions on Big Data*, 7(3):535–547, 2019.
28. D. Kang and A. Chan. Crowd counting by adaptively fusing predictions from an image pyramid. *arXiv preprint arXiv:1805.06115*, 2018.
29. L. Ke, M. Ye, M. Danelljan, Y. Liu, Y.-W. Tai, C.-K. Tang, and F. Yu. Segment anything in high quality. In *NeurIPS*, 2024.
30. B. Kerbl, G. Kopanas, T. Leimkühler, and G. Drettakis. 3d gaussian splatting for real-time radiance field rendering. *ACM Trans. Graph.*, 42(4):139–1, 2023.
31. J. Kim, M.-H. Jeon, S. Jung, W. Yang, M. Jung, J. Shin, and A. Kim. Transpose: Large-scale multispectral dataset for transparent object. *IJRR*, 43(6):731–738, 2024.
32. D. P. Kingma and J. Ba. Adam: A method for stochastic optimization. In *ICLR*, 2015.
33. A. Kirillov, E. Mintun, N. Ravi, H. Mao, C. Rolland, L. Gustafson, T. Xiao, S. Whitehead, A. C. Berg, W.-Y. Lo, et al. Segment anything. In *ICCV*, pages 4015–4026, 2023.
34. C. Lee, S. Park, H. Song, J. Ryu, S. Kim, H. Kim, S. Pereira, and D. Yoo. Interactive multi-class tiny-object detection. In *CVPR*, pages 14136–14145, 2022.
35. J. Li, W. Ji, M. Zhang, Y. Piao, H. Lu, and L. Cheng. Delving into calibrated depth for accurate rgb-d salient object detection. *IJCV*, 131(4):855–876, 2023.
36. T.-Y. Lin, P. Dollár, R. Girshick, K. He, B. Hariharan, and S. Belongie. Feature pyramid networks for object detection. In *CVPR*, pages 2117–2125, 2017.
37. T.-Y. Lin, P. Goyal, R. Girshick, K. He, and P. Dollár. Focal loss for dense object detection. In *ICCV*, pages 2980–2988, 2017.
38. L. Liu, K. Lin, S. Huang, Z. Li, C. Li, Y. Cao, and Q. Zhou. Instance segmentation for chinese character stroke extraction, datasets and benchmarks. *arXiv preprint arXiv:2210.13826*, 2022.
39. M. Liu, J. Dan, Z. Lu, Y. Yu, Y. Li, and X. Li. Cm-unet: Hybrid cnn-mamba unet for remote sensing image semantic segmentation. *arXiv preprint arXiv:2405.10530*, 2024.
40. W. Liu, X. Shen, C.-M. Pun, and X. Cun. Explicit visual prompting for low-level structure segmentations. In *CVPR*, pages 19434–19445, 2023.
41. X. Liu, L. Qi, Y. Song, and Q. Wen. Depth awakens: A depth-perceptual attention fusion network for rgb-d camouflaged object detection. *IVC*, 143:104924, 2024.
42. Y. Liu, Y. Tian, Y. Zhao, H. Yu, L. Xie, Y. Wang, Q. Ye, J. Jiao, and Y. Liu. Vmamba: Visual state space model. *NeurIPS*, pages 103031–103063, 2024.
43. Z. Liu, Y. Lin, Y. Cao, H. Hu, Y. Wei, Z. Zhang, S. Lin, and B. Guo. Swin transformer: Hierarchical vision transformer using shifted windows. In *CVPR*, pages 10012–10022, 2021.
44. Z. Liu, H. Mao, C.-Y. Wu, C. Feichtenhofer, T. Darrell, and S. Xie. A convnet for the 2020s. In *CVPR*, pages 11976–11986, 2022.
45. Z. Luo, N. Liu, W. Zhao, X. Yang, D. Zhang, D.-P. Fan, F. Khan, and J. Han. Vscope: General visual salient and camouflaged object detection with 2d prompt learning. In *CVPR*, pages 17169–17180, 2024.
46. J. Ma, F. Li, and B. Wang. U-mamba: Enhancing long-range dependency for biomedical image segmentation. *arXiv preprint arXiv:2401.04722*, 2024.
47. Z. Ma, X. Wei, X. Hong, and Y. Gong. Bayesian loss for crowd count estimation with point supervision. In *ICCV*, pages 6142–6151, 2019.
48. E. C. Magazine. Record year for ev sales: 17.1 million sold globally in 2024, 2024. Accessed: 2025-06-11.
49. Y. Pang, X. Zhao, T.-Z. Xiang, L. Zhang, and H. Lu. Zoom in and out: A mixed-scale triplet network for camouflaged object detection. In *CVPR*, pages 2160–2170, 2022.

50. Y. Pang, X. Zhao, T.-Z. Xiang, L. Zhang, and H. Lu. Zoomnext: A unified collaborative pyramid network for camouflaged object detection. *46(12):9205–9220*, 2024.
51. Y. Pang, X. Zhao, L. Zhang, and H. Lu. Multi-scale interactive network for salient object detection. In *CVPR*, pages 9413–9422, 2020.
52. Y. Pang, X. Zhao, L. Zhang, and H. Lu. Caver: Cross-modal view-mixed transformer for bi-modal salient object detection. *IEEE TIP*, 32:892–904, 2023.
53. Y. Pang, X. Zhao, J. Zuo, L. Zhang, and H. Lu. Open-vocabulary camouflaged object segmentation. In *European Conference on Computer Vision*, pages 476–495, 2024.
54. Y. Qian, L. Zhang, X. Hong, C. R. Donovan, O. Arandjelovic, U. Fife, and P. Harbin. Segmentation assisted u-shaped multi-scale transformer for crowd counting. 2022.
55. A. Radford, J. W. Kim, C. Hallacy, A. Ramesh, G. Goh, S. Agarwal, G. Sastry, A. Askell, P. Mishkin, J. Clark, et al. Learning transferable visual models from natural language supervision. In *ICML*, pages 8748–8763, 2021.
56. V. Ranjan, H. Le, and M. Hoai. Iterative crowd counting. In *ECCV*, pages 270–285, 2018.
57. N. Ravi, V. Gabeur, Y.-T. Hu, R. Hu, C. Ryali, T. Ma, H. Khedr, R. Rädle, C. Rolland, L. Gustafson, et al. Sam 2: Segment anything in images and videos. In *ICLR*, 2025.
58. S. Ren, K. He, R. Girshick, and J. Sun. Faster r-cnn: Towards real-time object detection with region proposal networks. In *NeurIPS*, 2015.
59. R. Rombach, A. Blattmann, D. Lorenz, P. Esser, and B. Ommer. High-resolution image synthesis with latent diffusion models. In *CVPR*, pages 10684–10695, 2022.
60. O. Ronneberger, P. Fischer, and T. Brox. U-net: Convolutional networks for biomedical image segmentation. In *MICCAI*, pages 234–241, 2015.
61. C. Ryali, Y.-T. Hu, D. Bolya, C. Wei, H. Fan, P.-Y. Huang, V. Aggarwal, A. Chowdhury, O. Poursaeed, J. Hoffman, et al. Hiera: A hierarchical vision transformer without the bells-and-whistles. In *ICML*, pages 29441–29454, 2023.
62. D. B. Sam and R. V. Babu. Top-down feedback for crowd counting convolutional neural network. In *AAAI*, number 1, 2018.
63. J. Shi et al. Good features to track. In *CVPR*, pages 593–600, 1994.
64. Z. Shi, J. Hu, J. Ren, H. Ye, X. Yuan, Y. Ouyang, J. He, B. Ji, and J. Guo. Hs-fpn: High frequency and spatial perception fpn for tiny object detection. In *AAAI*, volume 39, pages 6896–6904, 2025.
65. K. Simonyan and A. Zisserman. Very deep convolutional networks for large-scale image recognition. *arXiv preprint arXiv:1409.1556*, 2014.
66. V. A. Sindagi and V. M. Patel. Generating high-quality crowd density maps using contextual pyramid cnns. In *ICCV*, pages 1861–1870, 2017.
67. R. Strudel, R. Garcia, I. Laptev, and C. Schmid. Segmenter: Transformer for semantic segmentation. In *ICCV*, pages 7262–7272, 2021.
68. G. Sun, Z. An, Y. Liu, C. Liu, C. Sakaridis, D.-P. Fan, and L. Van Gool. Indiscernible object counting in underwater scenes. In *Proceedings of the IEEE/CVF Conference on Computer Vision and Pattern Recognition*, pages 13791–13801, 2023.
69. Z. Tian, C. Shen, H. Chen, and T. He. Fcos: Fully convolutional one-stage object detection. In *ICCV*, pages 9627–9636, 2019.
70. A. Vaswani, N. Shazeer, N. Parmar, J. Uszkoreit, L. Jones, A. N. Gomez, L. Kaiser, and I. Polosukhin. Attention is all you need. In *NeurIPS*, page 5998–6008, 2017.
71. J. Wan and A. Chan. Adaptive density map generation for crowd counting. In *ICCV*, pages 1130–1139, 2019.
72. Z. Wan, P. Zhang, Y. Wang, S. Yong, S. Stepputtis, K. Sycara, and Y. Xie. Sigma: Siamese mamba network for multi-modal semantic segmentation. pages 1734–1744, 2025.
73. A. Wang, H. Chen, L. Liu, K. Chen, Z. Lin, J. Han, et al. Yolov10: Real-time end-to-end object detection. *NeurIPS*, 37:107984–108011, 2024.
74. B. Wang, H. Liu, D. Samaras, and M. H. Nguyen. Distribution matching for crowd counting. In *NeurIPS*, pages 1595–1607, 2020.
75. J. Wang, M. Chen, N. Karaev, A. Vedaldi, C. Rupprecht, and D. Novotny. Vgggt: Visual geometry grounded transformer. In *CVPR*, pages 5294–5306, 2025.
76. X. Wang, X. Zhang, Y. Cao, W. Wang, C. Shen, and T. Huang. Seggpt: Towards segmenting everything in context. In *ICCV*, pages 1130–1140, 2023.
77. R. Watt. Scanning from coarse to fine spatial scales in the human visual system after the onset of a stimulus. *JOSA A*, 4(10):2006–2021, 1987.
78. H. Wei, X. Zhao, L. Lv, L. Zhang, W. Sun, and H. Lu. Growth simulation network for polyp segmentation. pages 3–15, 2023.
79. J. Wei, S. Wang, and Q. Huang. F³net: Fusion, feedback and focus for salient object detection. In *AAAI*, pages 12321–12328, 2020.
80. X. Wei, H. Wang, S. Ye, R. Luo, Y. Zhang, L. Gu, J. Dai, Y. Qiao, W. Wang, and H. Zhang. Point or line? using line-based representation for panoptic symbol spotting in cad drawings. *arXiv preprint arXiv:2505.23395*, 2025.
81. E. Xie, W. Wang, W. Wang, P. Sun, H. Xu, D. Liang, and P. Luo. Segmenting transparent objects in the wild with transformer. In *IJCAI*, pages 1194–1200, 2021.
82. E. Xie, W. Wang, Z. Yu, A. Anandkumar, J. M. Alvarez, and P. Luo. Segformer: Simple and efficient design for semantic segmentation with transformers. In *NeurIPS*, pages 12077–12090, 2021.
83. Z. Xing, T. Ye, Y. Yang, G. Liu, and L. Zhu. Segmamba: Long-range sequential modeling mamba for 3d medical image segmentation. In *MICCAI*, pages 578–588, 2024.
84. F. Xiong, X. Shi, and D.-Y. Yeung. Spatiotemporal modeling for crowd counting in videos. In *ICCV*, pages 5151–5159, 2017.
85. J. Xu, J. Ma, X. Zhao, H. Chen, B. Xu, and X. Wu. Detection technology for battery safety in electric vehicles: A review. *Energies*, 13(18):4636, 2020.
86. C. Yang, K. Zhuang, M. Chen, H. Ma, X. Han, T. Han, C. Guo, H. Han, B. Zhao, and Q. Wang. Traffic sign interpretation in real road scene. *arXiv preprint arXiv:2311.10793*, 2023.
87. M. Yang, K. Yu, C. Zhang, Z. Li, and K. Yang. Denseaspp for semantic segmentation in street scenes. In *CVPR*, pages 3684–3692, 2018.
88. X. Yuan, G. Cheng, K. Yan, Q. Zeng, and J. Han. Small object detection via coarse-to-fine proposal generation and imitation learning. In *ICCV*, pages 6317–6327, 2023.
89. A. Zareian, K. D. Rosa, D. H. Hu, and S.-F. Chang. Open-vocabulary object detection using captions. In *CVPR*, pages 14393–14402, 2021.

90. L. Zhang, A. Rao, and M. Agrawala. Adding conditional control to text-to-image diffusion models. In *ICCV*, pages 3836–3847, 2023.
91. Y. Zhang, D. Zhou, S. Chen, S. Gao, and Y. Ma. Single-image crowd counting via multi-column convolutional neural network. In *CVPR*, pages 589–597, 2016.
92. J.-X. Zhao, J.-J. Liu, D.-P. Fan, Y. Cao, J. Yang, and M.-M. Cheng. Egnnet: Edge guidance network for salient object detection. In *ICCV*, pages 8779–8788, 2019.
93. X. Zhao, S. Chang, Y. Pang, J. Yang, L. Zhang, and H. Lu. Adaptive multi-source predictor for zero-shot video object segmentation. *International Journal of Computer Vision*, pages 1–19, 2024.
94. X. Zhao, H. Jia, Y. Pang, L. Lv, F. Tian, L. Zhang, W. Sun, and H. Lu. M2snet: Multi-scale in multi-scale subtraction network for medical image segmentation. *arXiv preprint arXiv:2303.10894*, 2023.
95. X. Zhao, Y. Pang, Z. Chen, Q. Yu, L. Zhang, H. Liu, J. Zuo, and H. Lu. Towards automatic power battery detection: New challenge benchmark dataset and baseline. In *CVPR*, pages 22020–22029, 2024.
96. X. Zhao, Y. Pang, W. Ji, B. Sheng, J. Zuo, L. Zhang, and H. Lu. Spider: A unified framework for context-dependent concept segmentation. In *ICML*, pages 60906–60926, 2024.
97. X. Zhao, Y. Pang, L. Zhang, and H. Lu. Joint learning of salient object detection, depth estimation and contour extraction. *IEEE TIP*, 31:7350–7362, 2022.
98. X. Zhao, Y. Pang, L. Zhang, H. Lu, and L. Zhang. Suppress and balance: A simple gated network for salient object detection. In *ECCV*, pages 35–51, 2020.
99. X. Zhao, Y. Pang, L. Zhang, H. Lu, and L. Zhang. Towards diverse binary segmentation via a simple yet general gated network. *arXiv preprint arXiv:2303.10396*, 2023.
100. X. Zhao, L. Zhang, and H. Lu. Automatic polyp segmentation via multi-scale subtraction network. In *MICCAI*, pages 120–130, 2021.
101. H. Zhou, Y. Chang, H. Liu, W. Yan, Y. Duan, Z. Shi, and L. Yan. Exploring the common appearance-boundary adaptation for nighttime optical flow. *arXiv preprint arXiv:2401.17642*, 2024.
102. K. Zhou, Y. Wang, T. Lv, Y. Li, L. Chen, Q. Shen, and X. Cao. Explore spatio-temporal aggregation for insubstantial object detection: benchmark dataset and baseline. In *CVPR*, pages 3104–3115, 2022.
103. K. Zhou, Y. Wang, T. Lv, Q. Shen, and X. Cao. Gaseous object detection. *IEEE Transactions on Pattern Analysis and Machine Intelligence*, 2024.
104. T. Zhou, H. Fu, G. Chen, Y. Zhou, D.-P. Fan, and L. Shao. Specificity-preserving rgb-d saliency detection. In *CVPR*, pages 4681–4691, 2021.
105. T. Zhou, S. Ruan, and S. Canu. A review: Deep learning for medical image segmentation using multi-modality fusion. *Array*, 3:100004, 2019.
106. T. Zhou, Y. Zhou, K. He, C. Gong, J. Yang, H. Fu, and D. Shen. Cross-level feature aggregation network for polyp segmentation. *Pattern Recognition*, 140:109555, 2023.
107. L. Zhu, Z. Deng, X. Hu, C.-W. Fu, X. Xu, J. Qin, and P.-A. Heng. Bidirectional feature pyramid network with recurrent attention residual modules for shadow detection. In *ECCV*, pages 121–136, 2018.